From perception to action: Intracortical recordings reveal cortical gradients of human exogenous attention

Human exogenous attention relies on a cortical gradient of neural activity extending from perception to action

Tal Seidel Malkinson[*†1], Dimitri J. Bayle[2], Brigitte C. Kaufmann[1], Jianghao Liu[1,3], Alexia Bourgeois[4], Katia Lehongre[5], Sara Fernandez-Vidal[5], Vincent Navarro[1,6,7], Claude Adam[1,6,7], Virginie Lambrecq[1,6,7], Daniel S. Margulies[8], Jacobo D. Sitt[1], and Paolo Bartolomeo[1]

[1] Sorbonne Université, Inserm UMRS 1127, CNRS UMR 7225, Paris Brain Institute, ICM, Hôpital de la Pitié-Salpêtrière ; 75013 Paris, France
[2] Centre de Recherche sur le Sport et le Mouvement (CeRSM, EA 2931), Université Paris Ouest-La Défense ; 92000 Nanterre, France
[3] Dassault Systèmes, Vélizy-Villacoublay, France
[4] Laboratory of Cognitive Neurorehabilitation, Faculty of Medicine, University of Geneva; 1206 Geneva, Switzerland
[5] CENIR - Centre de Neuro-Imagerie de Recherche, Paris Brain Institute, ICM, Hôpital de la Pitié-Salpêtrière ; 75013 Paris, France
[6] Service de neurologie 1, Hôpital de la Pitié-Salpêtrière ; 75013 Paris, France
[7] Service de Neurophysiologie Clinique, Hôpital de la Pitié-Salpêtrière ; F-75013, Paris, France
[8] Laboratoire INCC, équipe Perception, Action, Cognition, Université de Paris ; 75005 Paris, France
* Corresponding author. Email: tal.seidel@mail.huji.ac.il

Summary

Exogenous attention, the process that makes external salient stimuli pop-out of a visual scene, is essential for survival. How attention-capturing events modulate processing dynamics in the human brain remains unclear. We obtained a comprehensive depiction of attentional cortical dynamics at high spatiotemporal resolution, by analyzing brain activity from 1,403 intracortical contacts implanted in 28 individuals, while they performed an exogenous attention task. The timing, location and task-relevance of attentional events defined a spatiotemporal gradient of three neural clusters, which mapped onto cortical core-periphery topography and presented a hierarchy of timescales, providing the scaffolding for attention temporal computations. Visual attributes modulated neural activity at one end of the gradient, while activity at the other end reflected the upcoming response timing, with attentional effects occurring at the intersection of visual and response signals. These findings reveal how the psychological construct of exogenous attention emerges over large-scale cortical gradients in the human brain.

Keywords

Attention, intracerebral recordings, cortical gradient, timescales, inhibition of return, response time, frontoparietal networks

Introduction

Imagine sitting in your car, waiting for the traffic light to change when suddenly an adjacent billboard sign starts flashing, capturing your attention. How would the flashing sign affect your ability to subsequently detect the light changing to green? In such a situation, the flashing automatically renders the sign more salient in the visual scene through a fast and dynamic orientation process known as exogenous attention.

---

† Further information and requests for resources and reagents should be directed to and will be fulfilled by the lead contact, Tal Seidel Malkinson (tal.seidel@mail.huji.ac.il).

Exogenous attention is a fundamental process that modulates response speed and perceptual sensitivity (Carrasco, 2011), and is prevalent among many vertebrate species (Gabay et al., 2013; Lev-Ari et al., 2020; Zhaoping, 2016), yet the expansion of attention systems in the human brain sets us apart (Patel et al., 2015). Understanding how our brain handles such salient distractions has become ever more crucial in our information-saturated modern environment. Yet, what exactly determines if our attention will be captured or reoriented away is not clear. Attention's temporal dimension, that is, how a previous stimulus such as a salient attention-capturing cue affects the processing of a subsequent stimulus, such as a target, is a key element for answering this important question. For instance, when successive stimuli appear at the same location within short delays, they lead to faster performance (response time (RT) facilitation). Slightly longer delays, however, slow down responses, a phenomenon termed inhibition of return (IOR), which may promote spatial exploration (Lupiáñez, 2010; Posner And Cohen, 1984). Under certain conditions (e.g. when cue and target do not overlap in time), IOR may even offset RT facilitation (Chica et al., 2014). These opposing RT modulations reflect underlying attentional processes (Shallice, 1979). However, the corresponding neural mechanisms remain uncertain. Despite decades of research, the nature and underlying neural mechanisms that mediate these attentional effects remain unclear (Lupiáñez et al., 2006; Martín-Arévalo et al., 2016). Evidence from human and non-human studies suggests that information about physical salience, which guides exogenous attention, may emerge as early as primary visual cortex, but this is still debated (Moore and Zirnsak, 2017; VanRullen, 2005). There are mixed results about the brain localization of such activities and the specific stimulus features that elicit exogenous attention (Burrows and Moore, 2009; Hegdé and Felleman, 2003; Wang et al., 2015). Salience information converges with top-down influences in several higher-order areas related to attention (Balan and Gottlieb, 2006; Itti and Koch, 2001; Moore and Zirnsak, 2017). In humans, attention-related networks include a dorsal frontoparietal network and a more right-lateralized ventral network, comprising the temporoparietal junction (TPJ) and the ventral prefrontal cortex (Corbetta and Shulman, 2002). Global salience may be computed within salience maps in the parietal cortex (Balan and Gottlieb, 2006; Buschman and Miller, 2007; Goldberg et al., 2006; Soltani and Koch, 2010) or the prefrontal cortex (Buschman and Miller, 2007; Moore and Armstrong, 2003; Thompson and Bichot, 2005), as well as in subcortical structures such as the superior colliculi and the pulvinar (Veale et al., 2017). Several of these areas, such as the superior colliculi, the frontal eye fields (FEF), the posterior parietal cortex, and their connections were also shown to be involved in IOR (Bourgeois et al., 2012, 2013a, 2013b; Dorris et al., 2002; Mirpour et al., 2009, 2019; Ro et al., 2003; Sapir et al., 1999; Siéroff et al., 2007). For example, dysfunction of these regions in the right hemisphere (Thiebaut de Schotten et al., 2005) causes spatial neglect, a condition characterized by a failure to orient attention to left-sided events and persistent RT facilitation instead of the typical IOR for right-sided targets (Bourgeois et al., 2012; Siéroff et al., 2007), linking abnormal exogenous attention to this disabling neurological condition. However, there is no consensus regarding the exact nature and neural basis of IOR (Lupiáñez et al., 2006, 2013) and very little effort was directed into exploring the neural basis of RT facilitation, with no single neural marker of these effects identified (Martín-Arévalo et al., 2016). Moreover, the methods used so far lacked sufficient spatiotemporal resolution to capture rapid attentional dynamics (e.g., human surface electroencephalography (EEG) and functional magnetic resonance imaging), or focused on isolated regions in non-human primate electrophysiology. Thus, our understanding of these attention processes stays fragmented, leaving the involved networks and underlying mechanism obscure.

Here we set out to establish the large-scale spatiotemporal neural dynamics of the mechanisms involved in the exogenous orienting of spatial attention. We used intracortical EEG (iEEG), a technique with unmatched spatiotemporal resolution in humans (Lachaux et al., 2003; Mukamel and Fried, 2012; Parvizi

and Kastner, 2018), acquired across 28 patients (1403 contacts), to achieve comprehensive cortical coverage. We aimed at studying how neural activity tracks visual, attentional and response aspects of the classic Posner exogenous attention task (Posner and Cohen, 1984), which allowed us to study the impact of attentional cues on the detection of subsequent targets, as a function of the delay between them. Typically, depending on the congruence between cue and target locations and the cue-target delay, this task generates differences in RT (RT facilitation or IOR) (Chica et al., 2014; Posner and Cohen, 1984). We assumed that the activity of putative neural mechanisms underlying these exogenous attention RT effects should present: 1) visual spatial sensitivity; 2) sensitivity to cue-target delay; 3) sensitivity to task relevance (cue/target); 4) association with RT.

To study how the evoked activity relates to large-scale brain organization, we examined its mapping across the cortical gradient, an axis of variance in anatomical, functional, neurodevelopmental and evolutionary features, along which areas fall in a spatially continuous order (Gao et al., 2020; Huntenburg et al., 2018; Margulies et al., 2016; Sydnor et al., 2021). The cortical gradient is a recently discovered organizing principle of cortical topography (Huntenburg et al., 2018; Margulies et al., 2016), based on the differentiation of connectivity patterns that captures a spatial and functional spectrum from early regions dedicated to perception and action (Periphery) to high-level regions of more abstract cognitive functions (Core) (Margulies et al., 2016), akin to Mesulam's (2000) unimodal-to-transmodal cortical hierarchy. Therefore, localizing activity along this gradient indicates the microstructural and genetic features, connectivity profile, and functional role of the activated region (Gao et al., 2020; Huntenburg et al., 2018).

Results

Twenty-eight participants undergoing presurgical evaluation of their epilepsy with iEEG (age 31.7 ± 8.1 years, 15 women, Table 1) performed the Posner peripheral cueing detection task (Posner and Cohen, 1984) (Fig. 1A). Participants were asked to press a central button as soon as a target (an X) appeared within a left- or right-sided placeholder box. A non-predictive peripheral cue (a 100-ms thickening of contour of one box) preceded the target with two possible stimulus onset asynchronies (SOA): 150ms (short-SOA), or 600ms (long-SOA), and appeared either on the same side of the target (Congruent trials) or opposite side (Incongruent trials) with equal probability.

Patients' performance was neurotypical (Lupiáñez, 2010; Posner and Cohen, 1984), with a 30-ms IOR effect (Fig. 1B; 2-way-ANOVA: SOA × Congruence interaction, $F_{(1,27)}=39.50$, $p<0.001$, $\eta^2 = 0.164$; post-hoc test: long-SOA congruent vs. Incongruent $p<0.001$). Congruent and incongruent RTs differed between SOAs (post-hoc tests: $p=0.047$ and $p=0.008$, respectively), but facilitation at short-SOA failed to reach significance (p=0.37; see Fig. S1 for individual RT effects and target-side analysis), as is often the case with this subtle effect (Chica et al., 2014). Moreover, left target Congruent RTs were slower tha Right target Congruent RTs, across both SOAs (Fig. S1B; repeated-measures 3-way ANOVA: Target-side X Congruence interaction- $F_{(1,27)}=8.28$, p=0.008, $\eta^2=0.007$), reflecting a Poffenberger effect (Anzola et al., 1977; Poffenberger, 1912), i.e. faster RTs for right cue & target than for left cue & target, when responding with the right hand. In Incongruent trials in which cue & target appear at opposite sides of the screen, this effect might have averaged out. No other Target-side effects reached significance, and IOR and RT facilitation effects did not significantly differ between left-sided and right-sided targets (paired samples t-test; IOR side: t(27)=1.83, p=0.077; RT Facilitation side: t(27)=1.68, p=0.11).

High-frequency broadband power (HFBB; 55-145Hz) was extracted from 1,403 usable contacts with bipolar montage, pooled across all participants (Fig. 1C; See Table 2 for detailed localization). Target-locked mean

normalized HFBB activity was computed for each contact in the eight experimental conditions (2x2x2 design: SOA x Congruence x Ipsilateral/Contralateral target relative to contact; Fig. 1C).

In order to reveal the main temporal patterns of activity that were sensitive to the experimental manipulations in a data-driven manner, we customized an unsupervised trajectory-clustering approach based on the k-means algorithm to cluster iEEG contacts according to their dynamic temporal patterns of activity across experimental conditions (Fig. S2). First, we selected responsive contacts, i.e. contacts with a significant effect in one condition or more, compared to baseline, which lasted at least 100ms, for inclusion in the clustering analysis. This resulted in 644 responsive contacts, for each of which we calculated the temporal trajectory in the 8-dimensional condition space (Congruent / Incongruent Trial X short-SOA / long-SOA X Ipsilateral / contralateral target), i.e. the path of each contact's HFBB over time across all experimental conditions. Each contact trajectory was then assigned to the cluster with the nearest trajectory-centroid, by iteratively minimizing within-cluster Manhattan distances. For further analyses, we used a k=6 solution, chosen using the Elbow method (see Fig. S2C and Fig. S3 for cluster number and stability, and Fig. S4A for the distribution of cluster contacts within participants).

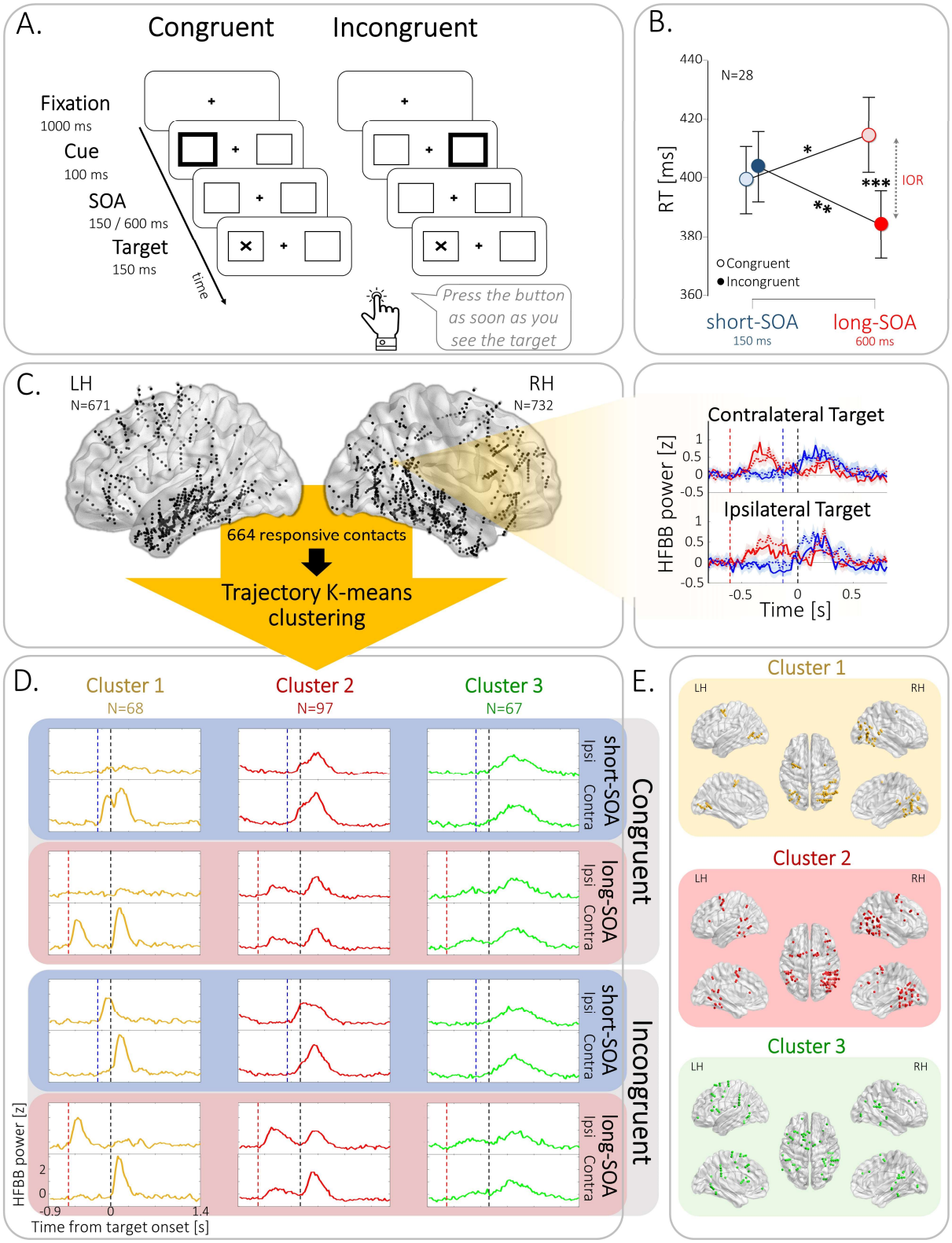

Figure 1 - *Neurotypical performance of implanted patients in the Posner task, contact localization and trajectory clustering.* ***(A)*** *Illustration of the Posner cued detection task. After 1000ms of fixation, a cue (thickened placeholder) appeared for 100ms at either side of the screen. On short SOA trials (short-SOA), the target ('X') occurred 150ms after cue onset; on long SOA trials (long-SOA)*

the target appeared 600ms after cue onset. The target appeared either on the same side of the screen as the cue (Congruent condition), or on the opposite site (Incongruent condition). Patients were required to press a central button with their right hand, as soon as the target appeared, while maintaining central fixation throughout stimuli presentation. Catch trials (n=24) had the same duration and cue presentation, but no target followed the cue. All trial types (n=336) were equiprobable and randomly interleaved. Stimuli are not drawn to scale. ***(B)*** *Patients' performance is neurotypical. * p=0.047; ** p=0.008; *** p<0.001. Error bars represent normalized SEM.* ***(C)*** *Left panel: Illustration of the localization of the contacts included in the analysis (black circles; N=1,403) in the left hemisphere (LH; N=671) and in the right hemisphere (RH, N=732), pooled across all patients. Each localization is the mean coordinates of the two contacts composing the contact's bipolar montage, depicted in normalized space (MNI152) for visualization. All included contacts were in grey matter or its immediate proximity. To reveal prototypical temporal patterns simultaneously across all conditions, the trajectories across the 8 condition dimensions of the mean high-frequency broadband (HFBB) target-locked activity of 664 significantly responsive contacts (significant time-point-by-time-point t-test for at least 100ms in one of the experimental conditions compared to baseline), were clustered using a novel trajectory K-means clustering approach. Right panel: Example of target-locked mean normalized HFBB responses of one contact in the right angular gyrus in Congruent (full lines) and Incongruent (dashed lines) trials, at short-SOA (blue) and long-SOA (red), with targets contralateral or ipsilateral to the contact. Dashed vertical lines represent target onset (black) and cue onset at short-SOA (blue) and long-SOA (red). Shaded areas represent SEM across trials for each sample.* ***(D)*** *Prototypical temporal profiles of contact clusters showing dynamic activity across experimental conditions: Trimmed-mean target-locked activity profiles of three contact clusters, across the 8 conditions (Congruent / Incongruent Trial X short-SOA / long-SOA X Ipsilateral target (Ipsi) / contralateral target (Contra)). The Cluster 1 (yellow) shows contralateral fast responses, with cue-target activity segregation at both SOAs; The Cluster 2 (red) shows bilateral slower responses with spatial sensitivity, with cue-target activity segregation at long-SOA but response integration in short-SOA; and the Cluster 3 (green) shows bilateral slowest responses with stimulus type sensitivity, with cue-target activity segregation at long-SOA but response integration at short-SOA. Dashed vertical lines represent target onset (black) and cue onset at short-SOA (blue) and long-SOA (red).* ***(E)*** *Clusters' spatial profile. Illustration of the localization of the contacts composing each cluster: Cluster 1 (yellow), Cluster 2 (red), Cluster 3 (green). For each cluster, dots represent contacts' localization in dorsal (middle), lateral (top) and medial (bottom) views of the right hemisphere (RH; right) and of the left hemisphere (LH; left).*

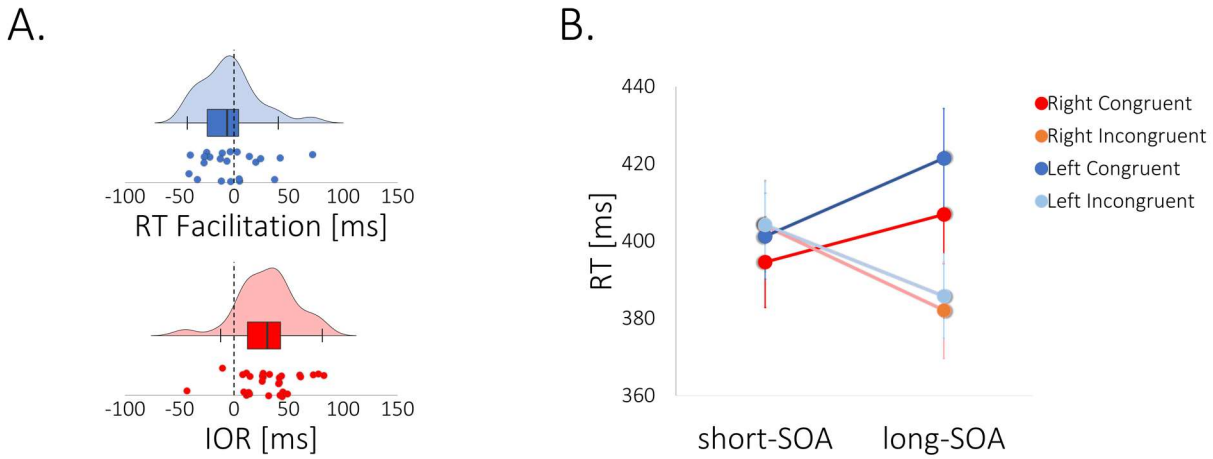

Figure S1 - *Behavioral effects.* ***(A)*** *Individual RT effects. Raincloud plots of patient RT difference between Congruent and Incongruent trials, in the short-SOA condition (RT Facilitation effect; top; blue dots) and in the long-SOA condition (IOR effect; bottom; red dots). Shaded areas represent RT distributions for long-SOA (shaded red) and short-SOA (shaded blue) conditions.* ***(B)*** *RT effects for right- & left-sided targets. Left target Congruent RTs were slower tha Right target Congruent RTs, across both SOAs (repeated-measures 3-way ANOVA: Target-side X Congruence interaction- $F_{(1,27)}$=8.28, p=0.008, η^2=0.007), reflecting the Poffenberger effect, i.e. faster RTs for right cue & target than for left cue & target, when responding with the right hand. In Incongruent trials in which cue & target appear at opposite sides of the screen, this effect might have averaged out. No other Target-side effects reached significance, and IOR and RT-facilitation effects did not significantly differ between left sided and right sided targets.*

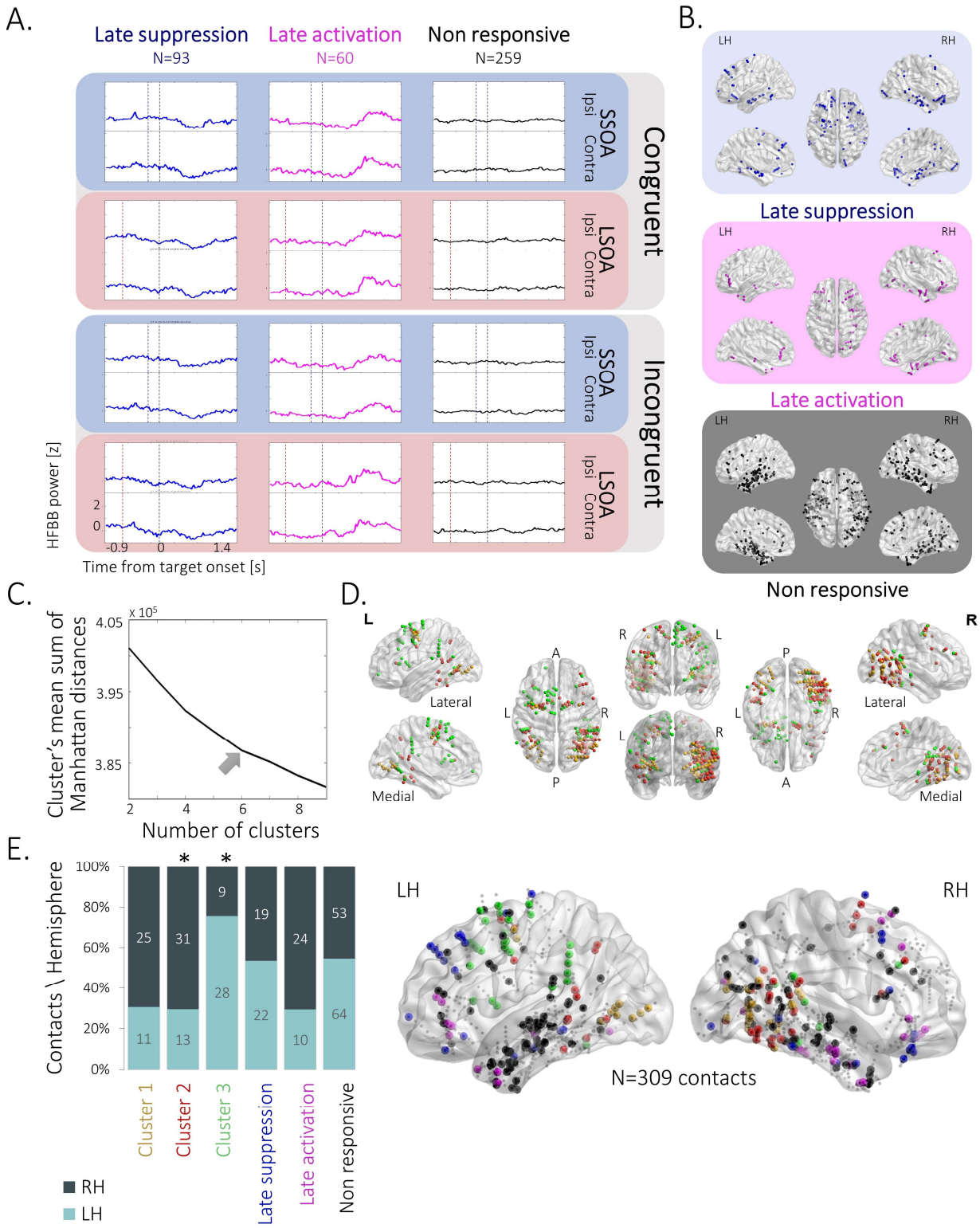

Figure S2 – Clusters' spatiotemporal profile. ***(A)*** *Prototypical activity profiles of contact clusters not included in the main analysis: Trimmed-mean target-locked activity profiles of Late suppression cluster (blue); Late activation cluster (magenta); Non responsive cluster (black), across the 8 conditions (Congruent / Incongruent X short-SOA / long-SOA X Ipsilateral target (Ipsi) / contralateral target (Contra)). Dashed vertical lines represent Target onset (black) and Cue onset at short-SOA (blue) and long-SOA (red)*

*conditions.**(B)** Spatial profile of clusters not included in the main analysis. Illustration of the localization of the contacts composing each cluster: Late suppression cluster (blue); Late activation cluster (magenta); Non responsive cluster (black). For each cluster, dots represent contacts' localization, computed as the mean coordinates of the two contacts composing each contact's bipolar montage, depicted in normalized space (MNI152) in dorsal (middle), lateral (top) and medial (bottom) views in the right hemisphere (RH; right) and the left hemisphere (LH; left). **(C)** Elbow method. Mean sum of Manhattan distances between each contact trajectory and its assign cluster trajectory for 2-9 clusters' solution. Maximal elbow (grey arrow) is observed at the 6-cluster solution. Clusters' hemispheric lateralization. **(D)** Relative localization of contacts of clusters 1,2 & 3 (yellow, red & green; correspondingly) visualized from different views. **(E)** Clusters' spatial distribution in symmetrically covered regions significantly differs between right and left hemispheres (dark grey & light grey respectively; $X^2_{(5)}=29.09$, $p<0.001$), resulting from a significant right lateralization of Cluster 2 (red) and a significant left lateralization of Cluster 3 (green; post hoc binomial tests, p=0.01 and p=0.003). Symmetrically covered regions were defined by calculating the overlap between the volumes of 3mm radius spheres around each contact for each hemisphere (see methods). Proportion of colors in each bar represent the percentage of contacts per hemisphere in each cluster; numbers are raw contact number per hemisphere in each cluster.*

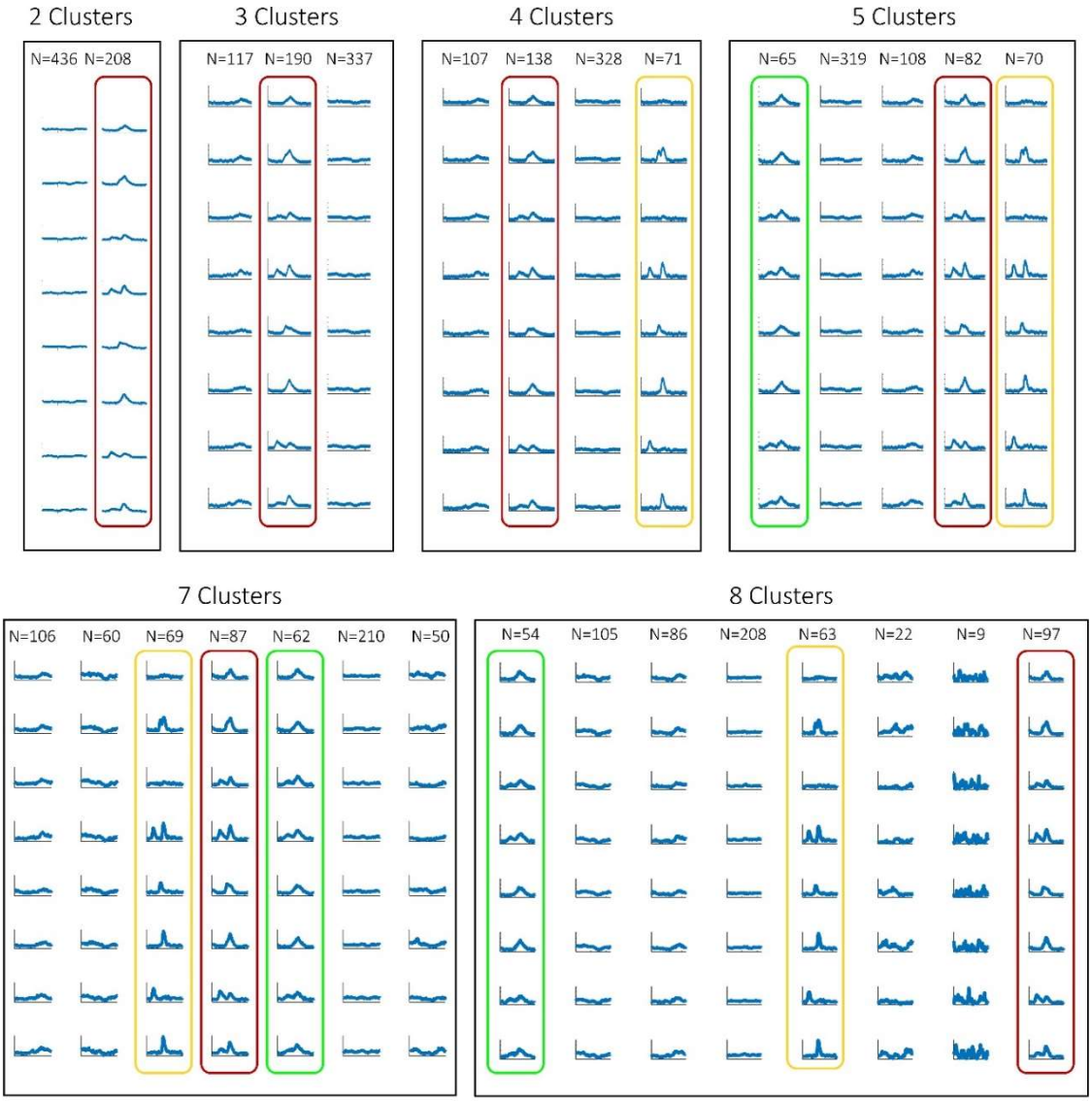

Figure S3 *– Trajectory k-means solution for different number of clusters. The three target-locked clusters analyzed in this study: The Cluster 1 (yellow), the Cluster 2 (red) and the Cluster 3 (green) are present from 5-cluster solution onward.*

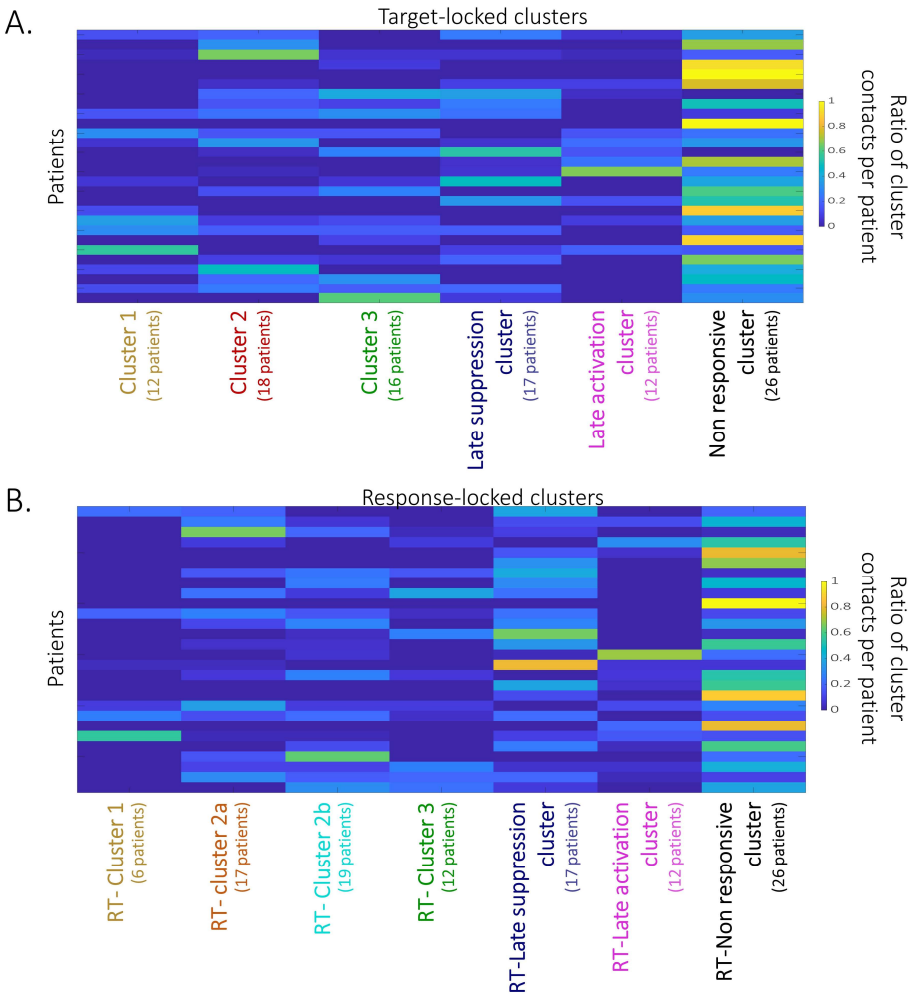

Figure S4 – Distribution of the cluster contacts within participants. ***(A)*** *The distribution of participants' contributions to target-locked clusters.* ***(B)*** *The distribution of participants' contributions to response-locked clusters. Each row represents one participant. Color code denotes the ratio of contacts in each cluster per participant.*

Out of the chosen 6-cluster solution (Fig. 1D-E, S2A-D), we focused on three clusters of contacts whose activity patterns changed across the experimental conditions (Fig. 1D) and were positively correlated to one another, whereas their correlation with the other three clusters was negative or near zero, indicating that these clusters form a distinct group (Fig. S5).

The first cluster (Cluster 1; 68 contacts from 12 patients; Fig. 1D left, S4) showed early responses only to contralateral cues and targets, and mainly consisted of contacts in the bilateral occipitotemporal cortex and in the prefrontal cortex, around the FEF (Fig. 1E top, S2D and Movie S1).

A second cluster (Cluster 2; 97 contacts from 18 patients; Fig. 1D middle) showed later ipsilateral and contralateral responses, with stronger responses to contralateral stimuli, demonstrating the spatial sensitivity of this cluster. Most contacts were in the caudal portion of the TPJ, around the angular gyrus, posterior temporal cortex and prefrontal cortex (Fig. 1E middle, S2D and Movie S1). The cluster was lateralized to the right hemisphere (Fig. S2E).

The third cluster (Cluster 3; 67 contacts from 16 patients; Fig. 1D right) was the last to react, with stronger responses to bilateral targets than to cues, hence suggesting a sensitivity to task-relevance. It was located mainly in the rostral TPJ region (around the supramarginal gyrus), posterior temporal cortex and prefrontal cortex (Fig. 1E bottom, S2D and Movie S1), and was lateralized to the left hemisphere (Fig. S2E). Importantly, the response in Clusters 2 and 3 was sensitive to the cue-target delay. For the short-SOA, cue and target responses summed together, but they were segregated for the long-SOA. Activity in the three remaining clusters did not seem to vary across experimental conditions, with one cluster showing late inhibition, one showing late activation and one showing no response (see Fig. S2A).

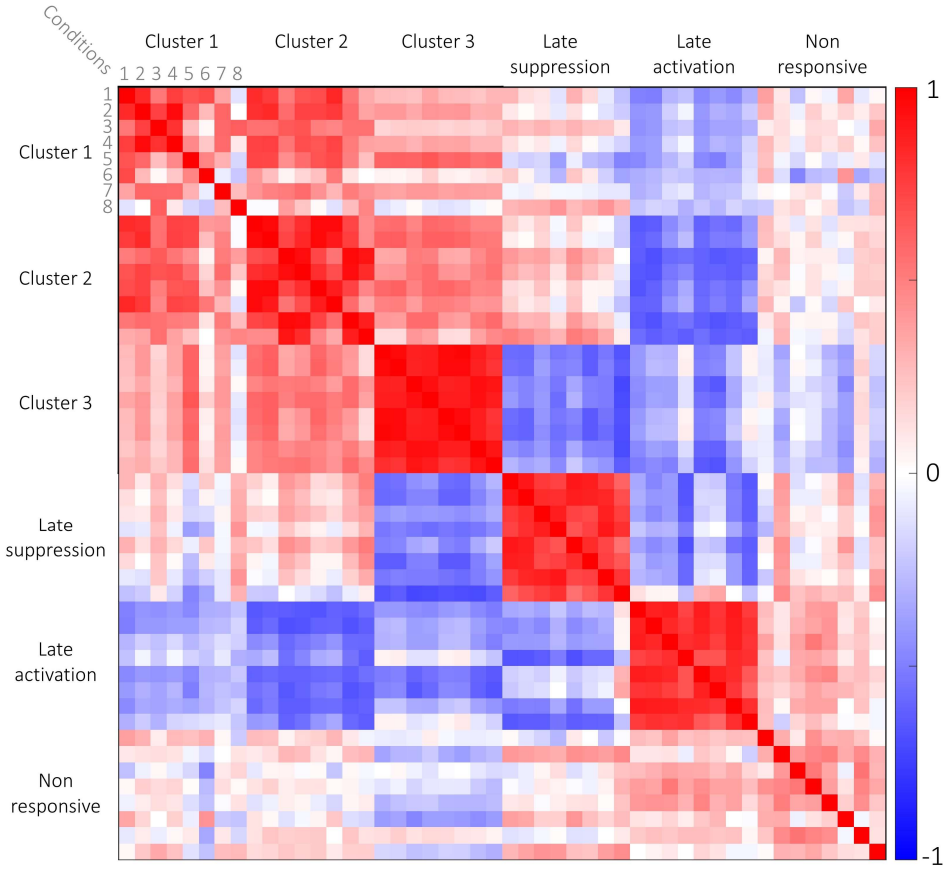

Figure S5 – Clusters 1, 2 & 3 form a distinct group among all clusters. Pearson correlations between condition centroid time-series across target-locked clusters reveal that the correlations of – Clusters 1, 2 & 3 vary across experimental conditions within each cluster and positively correlate between these clusters. The correlation pattern within the three other clusters is more uniform, and negatively correlated across clusters. Color bar represents the r coefficient (negative correlation – blue; positive correlation-red); Numbers correspond to the experimental conditions (1- Contralateral target short-SOA Congruent; 2- Contralateral target short-SOA Incongruent; 3-'Contralateral target long-SOA Congruent; 4-Contralateral long-SOA Incongruent; 5-Ipsilateral target short-SOA Congruent; 6-Ipsilateral target short-SOA Incongruent; 7-Ipsilateral target long-SOA Congruent; 8-Ipsilateral target long-SOA Incongruent).

We then went on to study the way neural activity in these clusters relates to attentional, visual and response aspects of the task. We first explored how our experimental manipulation of attentional events influenced the clusters' target-locked neural activity. Specifically, we examined the neural correlates of the behaviorally significant IOR effect, by comparing long-SOA Congruent and Incongruent trials in the cue

time-window (-600-0ms) and in the target time-window (0-800ms; time-resolved 3-way ANOVA with Congruence, Target Laterality and Contact Hemisphere as factors; Fig. 2, See Tables S1 & S2 for full results).

In the cue time-window, Congruent and Incongruent trials did not significantly differ overall (no significant main Congruence effect; Fig. S6), reflecting the fact that the cue location did not predict the congruence of the upcoming target. Instead, there were mainly neural effects reflecting the differential lateralization of cues preceding Congruent and Incongruent targets (See Supplementary material).

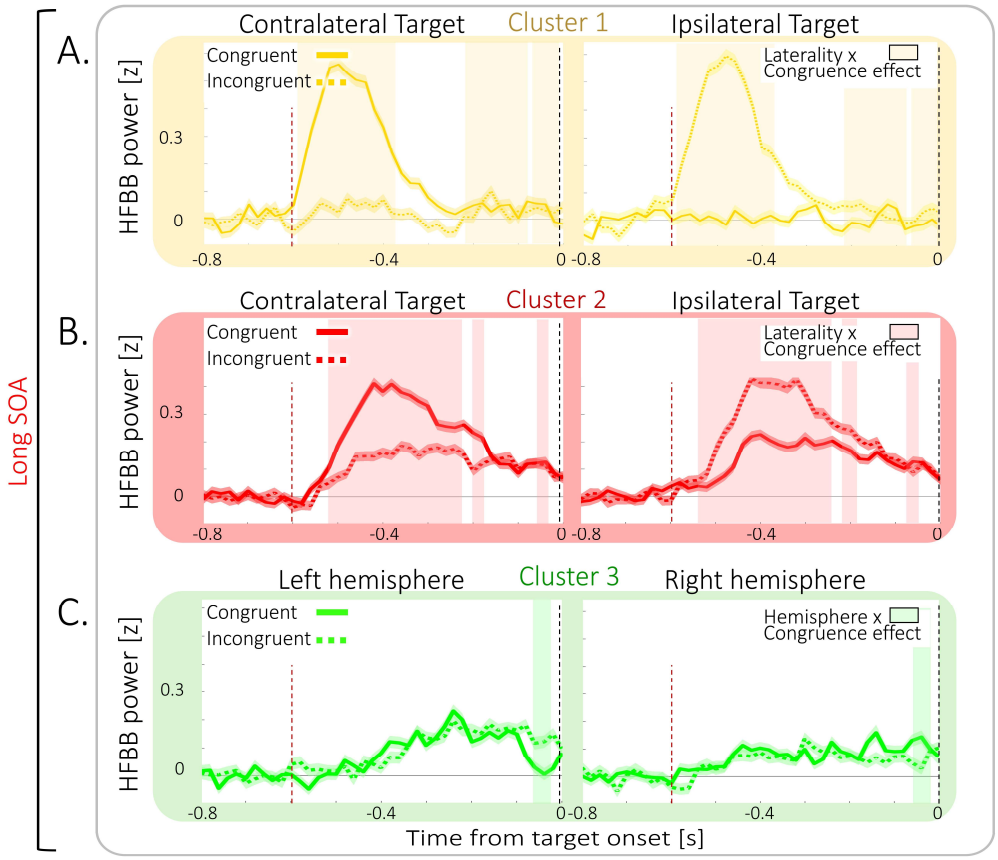

Figure S6 – Congruence-related neural activity in the Cue time-window. Mean target-locked LSOA activity in Cluster 1 (yellow), Cluster 2 (red) and Cluster 3 (green), computed over trials pooled across all cluster contacts, for Congruent trials (full lines) and Incongruent trials (dashed lines) in the long-SOA. ***(A)*** *In Cluster 1 a significant Laterality x Target-congruence effect was observed (yellow shaded area; largest p=0.018) showing it responds only to contralateral cues.* ***(B)*** *In Cluster 2 responses were stronger to contralateral cues than to ipsilateral ones, as shown by a significant Laterality x Target-congruence effect (shaded red areas; largest p=0.038).* ***(C)*** *Cluster 3 showed a significant Hemisphere x Target-congruence (green shaded area; largest p=0.045).* ***(A)-(C)*** *Shaded areas around traces depict SEM; Dashed vertical lines represent Target onset (black) and Cue onset (red).*

In the target time-window, cluster 2 showed a Congruence main effect at the offset of the target-related activity (240-300ms post target; largest p=0.002; see Fig. 2D for examples of single contacts). Moreover, in the contacts of this cluster in the right hemisphere, the response peaked 22ms later in the Congruent than in the Incongruent trials (140-220ms post target onset; Hemisphere x Congruence interaction: largest p=0.03; post hoc tests: largest p=0.014), mirroring behavioral IOR. There were no congruence effects in Cluster 1 (Fig. 2A) and in Cluster 3 there was only a late Congruence effect at 660-680ms post-target (largest p=0.003). Therefore, IOR-related activity was mainly restricted to the Cluster 2, thus attentional events corresponded to the neural dynamics of this cluster.

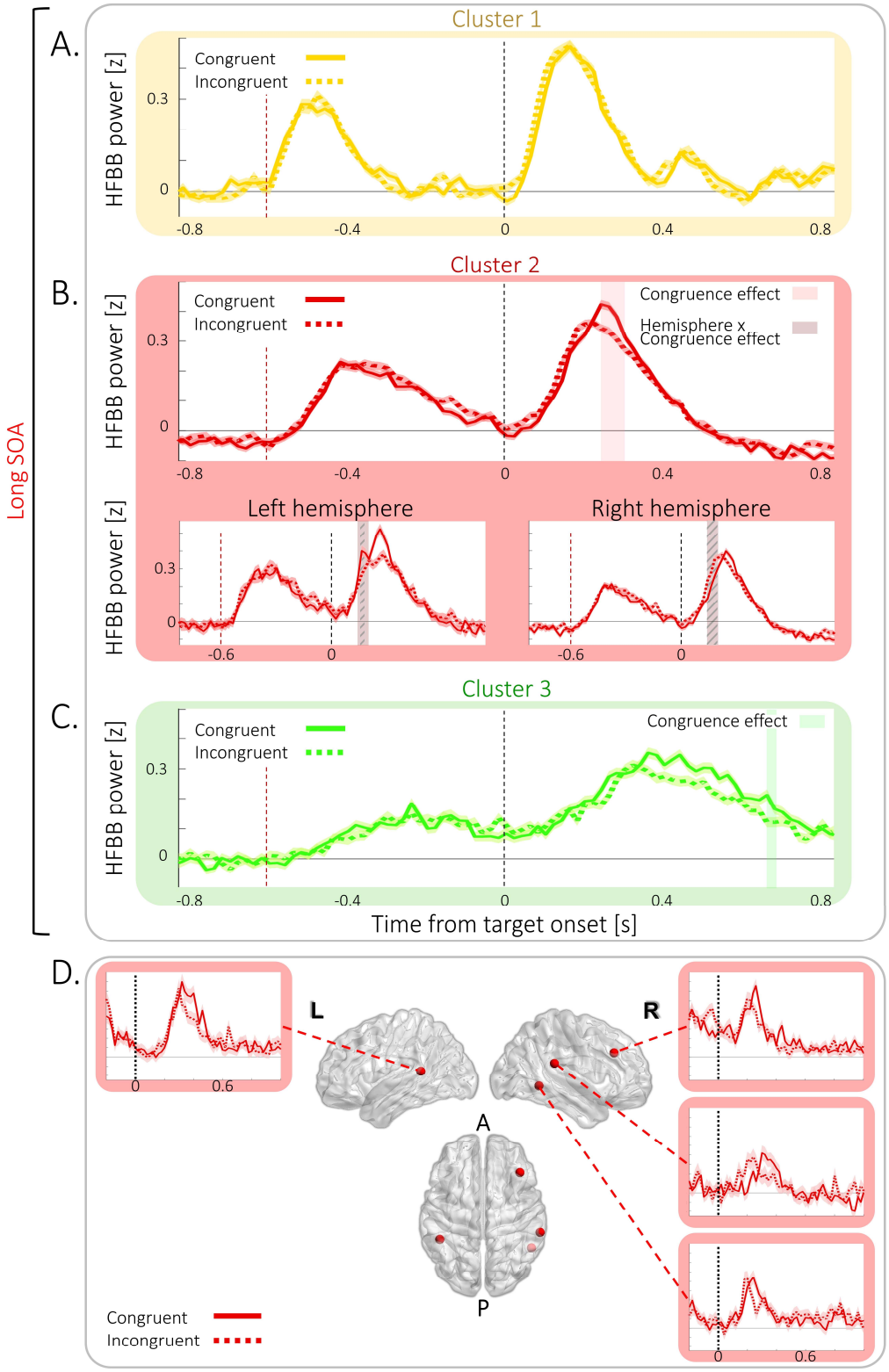

Figure 2 - IOR-related neural activity. Mean target-locked long-SOA activity in Cluster 1 (yellow), Cluster 2 (red) and Cluster 3 (green), computed over trials pooled across all cluster contacts, for Congruent trials (full lines) and Incongruent trials (dashed lines). ***(A)*** *In the Cluster 1, no significant Congruence effect was observed.* ***(B)*** *In Cluster 2 activity in Congruent and Incongruent trials (IOR-related) differed significantly at 0.24-0.3s post target (shaded red areas; Congruence main effect: largest p=0.002), and a significant*

hemispheric difference between IOR-related responses was observed at 0.14-.022s post target (shaded brown area; Hemisphere x Congruence interaction: largest p=0.03; Diagonally striped areas represent significant Congruence x Hemisphere post hoc comparisons (p<0.05)). ***(C)*** *In Cluster 3 activity in Congruent and Incongruent trials differed significantly at 0.66-0.68s post target (green shaded area; Congruence main effect: largest p=0.003). A-C. Shaded areas around traces depict SEM; Dashed vertical lines represent Target onset (black) and Cue onset (red) at the long-SOA Condition.* ***(D)*** *Representative examples of HFBB power IOR-related activity in the Congruent (full line) & Incongruent (dashed line) long-SOA conditions of individual contacts of the Cluster 2. p values are Holm corrected.*

How do these clusters of neural activity relate to the manual response? We examined whether cluster neural dynamics relate to motor response timing, across experimental conditions, reflecting the significant RT differences between SOAs in the Congruent and Incongruent conditions. In each cluster, we divided the trials (pooled across conditions) into 20 quantiles according to their RT (Fig. 3A), and tested the relation of RT-bins with the neural activity using a time-resolved 1-way repeated measures ANOVA (See Fig. 3B-C for results and examples of single contacts). In Cluster 2, the offset of the target-related activity differed across RT bins (300-560ms post target; largest p=0.028), with a faster decay at faster RT-bins, just before the motor response. In Cluster 3, a RT-bin effect occurred around the peak of target-related activity and button-press time (280-300 and 400-420ms post target; largest p=0.007). In Cluster 1, a RT-bin effect occurred at 500-540 and 560-680ms post target onset (p<0.002), suggesting a RT-related late modulation after response offset and button press time. RT-related target-locked activity in Clusters 2 and 3 was confirmed by cross-correlation analysis (Fig. S7), which revealed that only in these clusters, did the temporal dynamics of neural activity shift according to RTs, and that this shift correlated with RTs. Thus, neural activity in Clusters 2 and 3 was related to the timing of the upcoming motor response, reflecting the behavioral outcome of the task and its associated neural processes.

We next studied the neural correlates of the visual aspects of the Posner task, by adopting a complementary approach and examining visual modulation of response-locked activity. We applied the trajectory k-means clustering analysis to response-locked activity (Fig. S8 A-C and Movie S2). To map the correspondence of the seven response-locked clusters to the previously identified target-locked clusters, we performed a contingency analysis that revealed four corresponding response-locked clusters ($X^2_{(30)}$=1442; p <0.001; Contingency coefficient 0.83; Fig. 3 and S8D). Specifically, this locking-activity to the response further separated the clusters: RT-Cluster 1 (46 contacts; 60.3% of target-locked Cluster 1), RT-Cluster 2a (85 contacts; 35.3% of target-locked Cluster 1 and 49.5% Cluster 2), RT-Cluster 2b (79 contacts; 46.4% of target-locked cluster 1 and 31.3% of Cluster 2), and RT-Cluster 3 (39 contacts; 50.7% of target-locked Cluster 3). We repeated the RT-binning analysis, as described above (Fig. 3D), and tested the RT-bin effect on the neural activity using a time-resolved 1-way repeated measures ANOVA (See Fig. 3E-F for results and examples of individual contacts). Because RT is defined as the time from target onset to the response, this procedure sorted the response-locked trials according to target onset, and thus could unveil visual modulation of response-locked activity. The onset of the response-locked activity was modulated by target onset only in RT-Cluster 1 (120-100ms pre-response; largest p=0.04) and RT-Cluster 2a (700-680ms, 520-500ms, 300-200ms pre-response; largest p=0.004). In RT-Cluster 2b and RT-Cluster 3, neural activity peak was aligned to the response without significant visual modulation. The visual modulation of response-locked activity in RT-Cluster 1 and RT-Cluster 2a was confirmed by a cross-correlation analysis (Fig. S9), which revealed that only for contralateral targets in these clusters the temporal dynamics of neural activity was shifted according to target-onset and this shift correlated with target-onset time. Thus, response-locked activity revealed that only the clusters with early response-locked activity showed visual modulation, while clusters with later activity were only sensitive to the timing of the motor response.

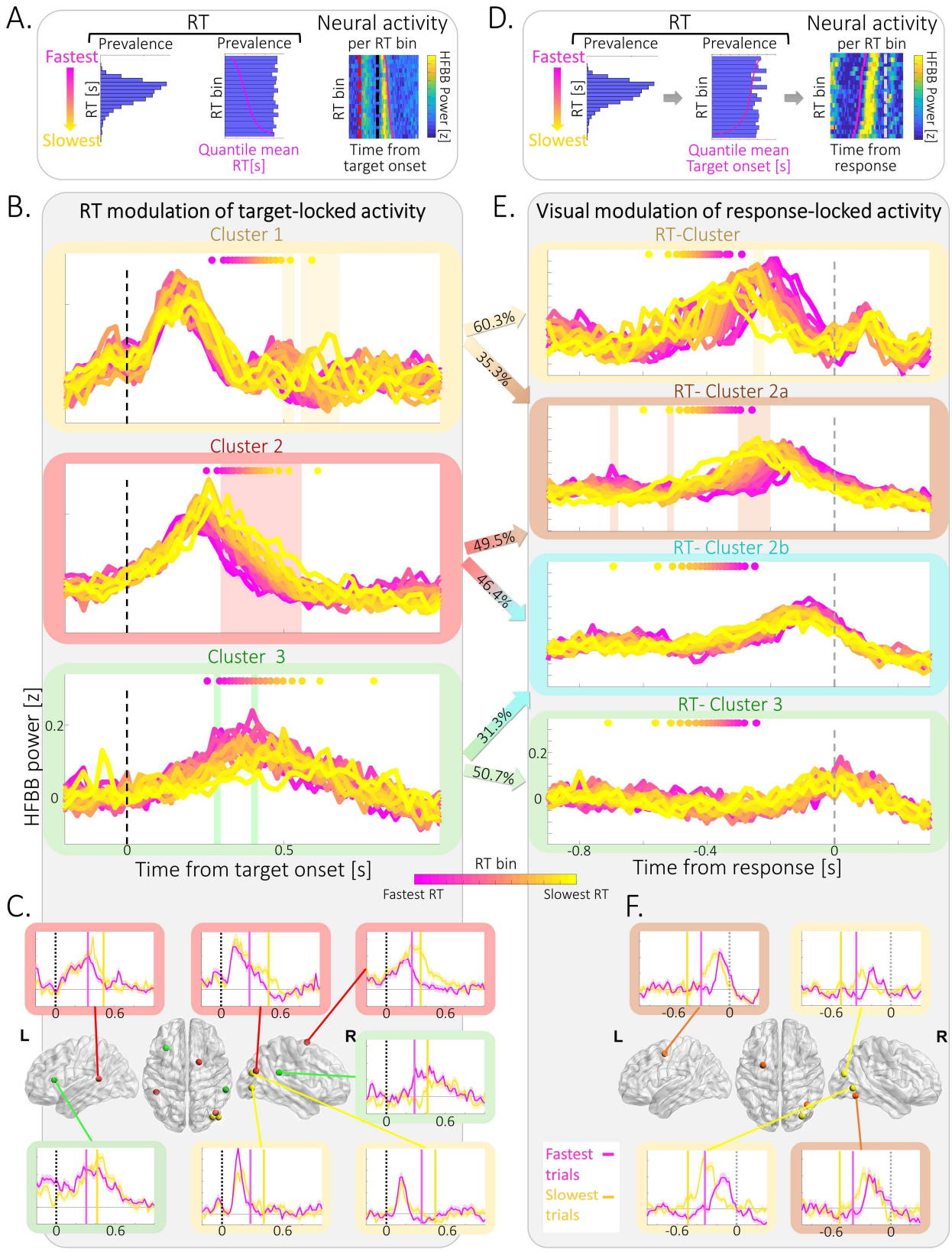
A.
RT
Neural activity
Prevalence
Prevalence
per RT bin
Fastest
RT [s]
Slowest
RT bin
RT bin
HFBB Power [z]
Quantile mean RT[s]
Time from target onset
D.
RT
Neural activity
Prevalence
Prevalence
per RT bin
Fastest
RT [s]
Slowest
RT bin
RT bin
HFBB Power [z]
Quantile mean Target onset [s]
Time from response
B.
RT modulation of target-locked activity
Cluster 1
Cluster 2
Cluster 3
HFBB power [z]
0.2
0
0
0.5
Time from target onset [s]
60.3%
35.3%
49.5%
46.4%
31.3%
50.7%
E.
Visual modulation of response-locked activity
RT-Cluster
RT- Cluster 2a
RT- Cluster 2b
RT- Cluster 3
0.2
0
-0.8
-0.4
0
Time from response [s]
RT bin
Fastest RT
Slowest RT
C.
0
0.6
L
R
F.
-0.6
0
L
R
Fastest trials
Slowest trials

Figure 3 - RT & visual modulation of Target-locked & Response-locked Neural activity. ***(A)*** *Schematic illustration of the procedure for computing neural activity at different RT bins: Within each cluster, the trial distribution of RTs across all conditions (left) was divided into 20 quantiles (RT bins; middle). RT bins were ordered according to their mean RT (magenta line), and the quantile's mean target-locked neural activity pooled across cluster contacts, was computed (right; Vertical dashed lines denote Cue (red) & target (black) onset; magenta line represent mean RT).* ***(B)*** *RT modulates target-locked neural activity (pooled across conditions; color coded from fastest (Magenta) to slowest (yellow) RT bin; Dashed vertical black line represents Target onset; Color-coded dots at the top of each panel represent mean RT for each RT bin (pink – fastest RT to yellow – slowest RT)). Top: Late RT modulation of activity in Cluster 1 (yellow): Main effect of RT bin was observed at 0.5-0.54 & 0.56-0.68s post target onset (shaded yellow area; largest p=0.002), suggesting RT-related late modulation after response offset & button press time. Middle: RT modulation of neural response offset and button press time in Cluster 2 (red): Main effect of RT bin was observed at 0.3-0.56s post target onset (shaded red area; largest p=0.028), suggesting RT modulation of response offset. Bottom: RT modulation of response in Cluster 3 (green): Main effect of RT bin occurred at 0.28-0.3 and 0.4-0.42s post target onset (shaded green area; largest p=0.007), suggesting RT modulation around neural response peak and button-press time.* ***(C)*** *Examples of single contact HFBB power activity in the fastest (pink) & slowest (yellow) third of all trials of the three target-locked clusters. Vertical dashed black lines represent target onset; Vertical full lines denote mean RT for fastest (magenta) & slowest (yellow) trials.* ***(D)*** *Schematic illustration of the procedure for computing neural response-locked activity at different RT bins: Within each cluster, the trial distribution of RTs in each condition (left) was divided into 20 quantiles (RT bins; middle). RT bins were ordered according to their mean RT, corresponding to target onset time (magenta line). Then, each quantile's mean Response-locked neural activity pooled across all cluster contacts was computed (right; Vertical grey dashed line denote RT (black) onset; magenta line represent mean target onset time).* ***(E)*** *Visual modulation of response-locked neural activity (pooled across conditions; color coded from fastest (Magenta) to slowest (yellow) RT bin; Dashed vertical grey line represents RT; Color-coded dots at the top of each panel represent mean target onset time for each RT bin (pink – fastest RT to yellow – slowest RT)). Top: Target onset time modulates activity in the RT-Cluster 1 (yellow): Main effect of RT-bin was observed at 0.12-0.10s pre-response (shaded yellow area; largest p=0.04). Target onset time modulates activity in the RT-Cluster 2a (orange): Main effect of RT bin was observed at 0.70-0.68s, 0.52-0.50s & 0.30-0.20s pre-response (shaded orange area; largest p=0.004). No significant modulation of activity in the RT-Cluster 2b (turquoise) & the RT-Cluster 3 (green) by target onset time. Arrows between panels (B) & (E) denote the contingency between Target-locked & Response-locked clusters (% electrodes of each Target-locked cluster assigned to each Response-locked cluster; see Fig. S8).* ***(F)*** *Examples of single contact HFBB power activity in the fastest (pink) & slowest (yellow) third of all trials of RT-Cluster 1 and RT-Cluster 2a. Vertical dashed grey lines represent RT; Vertical full lines denote mean target onset time for fastest (magenta) & slowest (yellow) trials. p* values are Holm corrected.

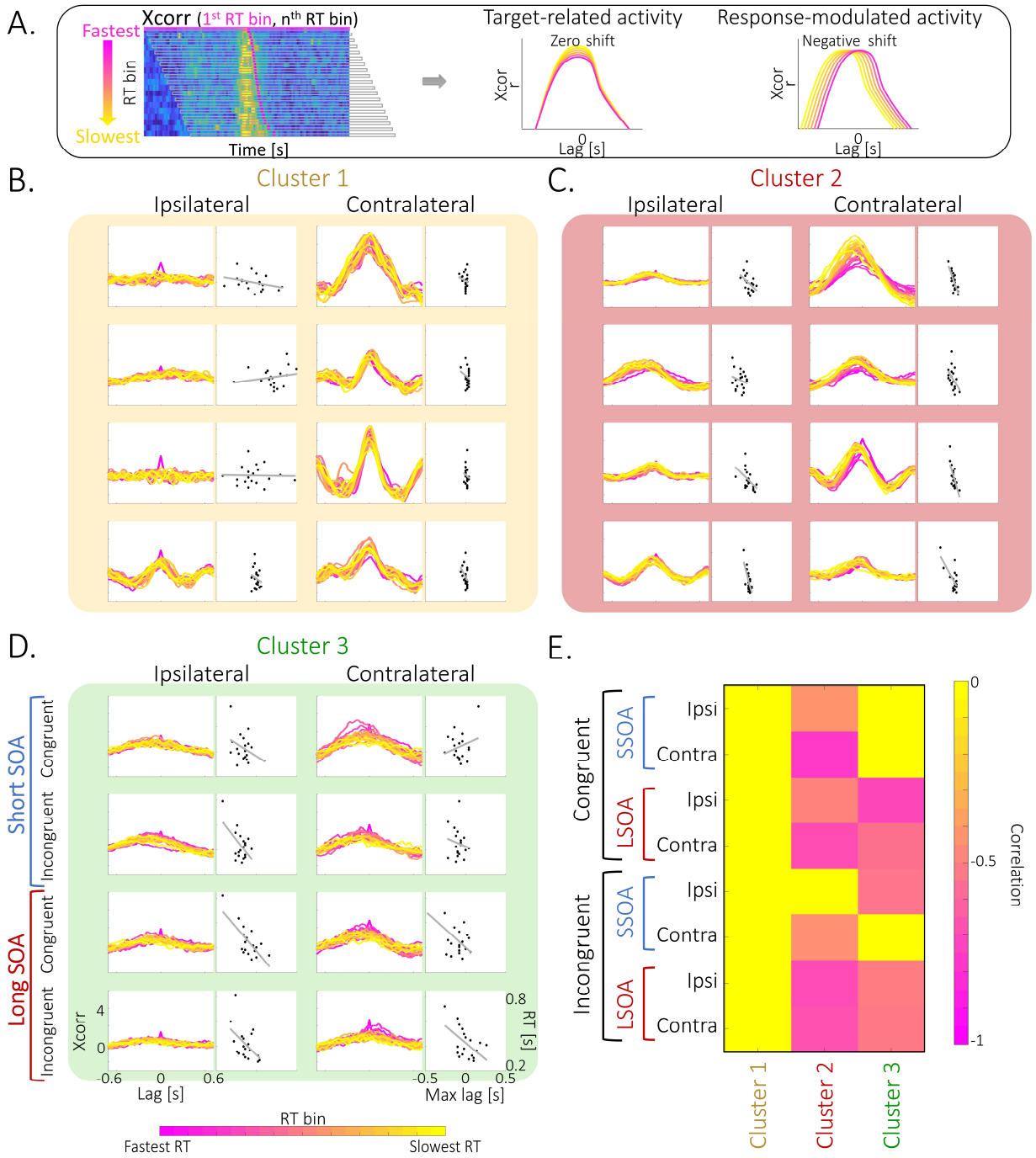

Figure S7 – Cluster neural target-locked activity timing is correlated with behavior. ***(A)*** *Schematic illustration of the procedure for computing the cross-correlation (Xcorr) of neural activity across RT bins: Cross-correlation between target-locked activity at the fastest RT bin and all subsequent bins was computed (left). If cluster activity is target-associated, maximal cross-correlation will be centered on target onset, resulting in a zero shift across all RT bins (middle). If cluster activity is response-associated, maximal cross-correlation will follow the RT, resulting in a negative shift of cross-correlation lag (right).* ***(B)-(D)****. Cross-correlogram of neural activity at different RT bins (pink- fastest RT; yellow - slowest RT) as a function of cross-correlation lag (left columns) and Pearson correlation (grey line) between maximal cross-correlation lags (Max lag) and bin's mean RTs (right columns), across the 8 conditions (Congruent / Incongruent X short-SOA / long-SOA X Ipsilateral target / contralateral target) in Cluster 1 (yellow), Cluster 2 (red) and Cluster 3 (green).* ***(B)*** *Cluster 1 activity is target-associated: Cross-correlation plots are centered on zero, especially for contralateral targets.*

(C) *Activity in Cluster 2 is response-associated: Cross-correlation plots show a negative shifted lag that is generally correlated with RT.* ***(D)*** *Cluster 3 activity is response-associated: Cross-correlation plots show a negative shifted lag, correlated with RT under certain conditions.* ***(E)*** *Significant negative correlation between cross-correlation maximal lag and bin mean RT in Clusters 2 & 3: significant ($p<0.05$) negative correlations were found only in these two clusters.*

A.

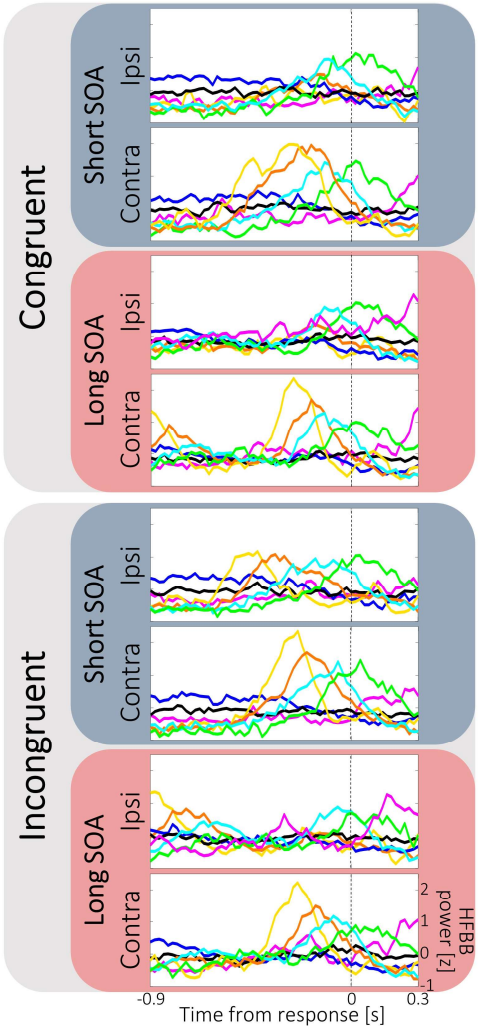

B.

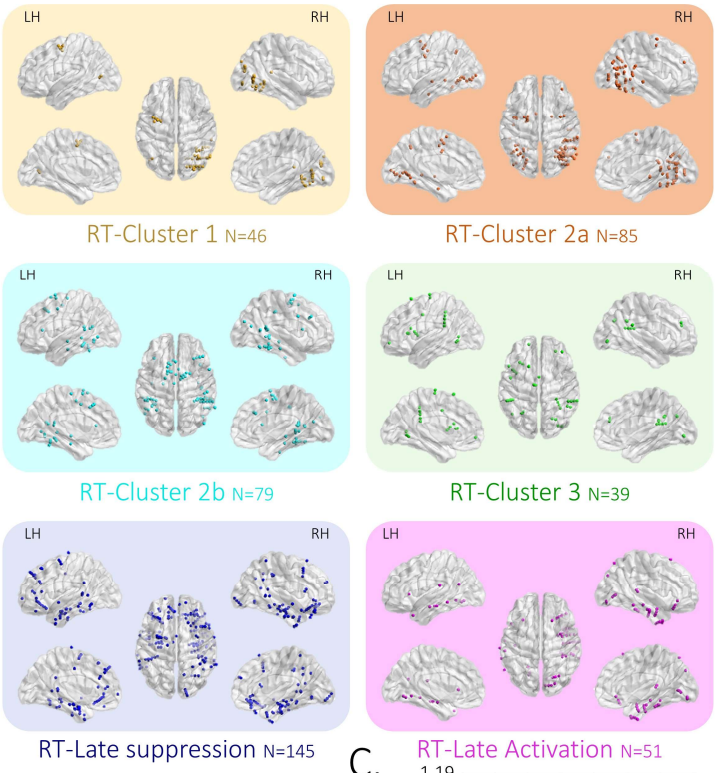

C.

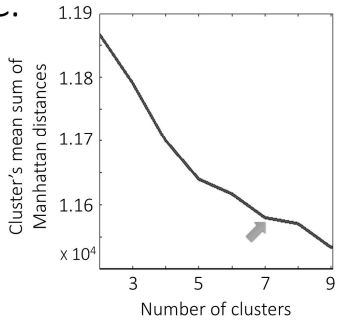

D.

Response-locked clusters

Target-locked clusters	RT-Cluster 1	RT-Cluster 2a	RT-Cluster 2b	RT-Cluster 3	RT-Late suppression	RT-Late Activation	RT-Non responsive	Total
Cluster 1	41 60.3%	24 35.3%	0 0%	0 0%	0 0%	1 1.5%	2 2.9%	68 100%
Cluster 2	1 1%	48 49.5%	45 46.4%	1 1%	2 2.1%	0 0%	0 0%	97 100%
Cluster 3	0 0%	4 6%	21 31.3%	34 50.7%	0 0%	5 7.5%	3 4.5%	67 100%
Late suppression	2 2.2%	0 0%	0 0%	0 0%	82 88.2%	0 0%	8 8.6%	60 100%
Late activation	1 1.7%	0 0%	0 0%	1 1.7%	14 23.3%	31 51.7%	13 21.7%	60 100%
Non responsive	1 0.4%	9 3.5%	12 4.6%	3 1.2%	47 18.1%	14 5.4%	173 66.8%	259 100%

Figure S8 *– Response-locked clusters' spatiotemporal profile.* ***(A)*** *Trimmed-mean Response-locked activity profiles of the seven contact clusters across the 8 conditions (Congruent / Incongruent X short-SOA / long-SOA X Ipsilateral target / contralateral target): RT-Cluster 1 (yellow); RT-Cluster 2a (orange); RT- Cluster 2b (turquoise); RT-Cluster 3 (green); RT-Late suppression cluster (blue); RT-Late activation cluster (magenta); RT-Non responsive cluster (black). Dashed vertical line represents motor response time.* ***(B)*** *Response-locked clusters' spatial location. Illustration of the localization of the contacts composing each cluster (colors as in A). For each cluster, dots represent contacts' localization, computed as the mean coordinates of the two contacts composing each contact's bipolar montage, depicted in normalized space (MNI152) in dorsal (middle), lateral (top) and medial (bottom) views in the right hemisphere (RH) and the left hemisphere (LH).* ***(C)*** *Elbow method. Mean sum of Manhattan distances between each contact trajectory and its assigned cluster trajectory for 2-9 clusters' solution. Maximal elbow (grey arrow) is observed at 7-cluster solution.* ***(D)*** *Contingency table showing the mapping between target-locked and response-locked clusters. The distribution of target-locked clusters' contacts (rows; number of contacts & % within row) across the different response-locked clusters (columns) was significantly different than chance (p <0.001; Contingency coefficient =0.83).*

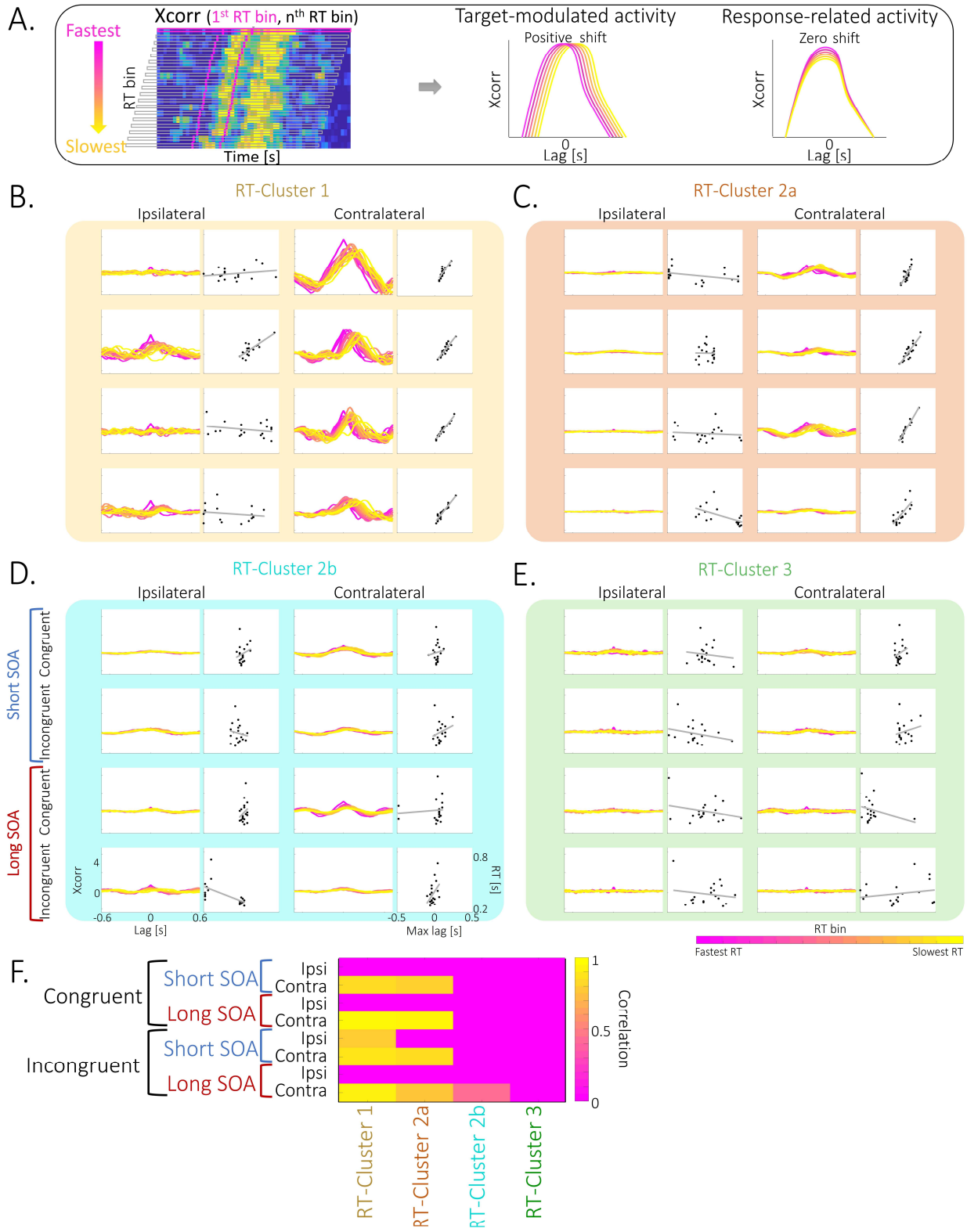

Figure S9 – Correlation of cluster response-locked neural activity with visual processing. ***(A)*** *Schematic illustration of the procedure for computing the cross-correlation (Xcorr) between response-locked neural activity across RT bins: Cross-correlation between response-locked activity at the fastest RT bin and all subsequent bins was computed (left; magenta lines depict mean Cue and Target*

onset times). If cluster activity is target-associated, maximal cross-correlation will follow the RT (here indicative of quantile's mean target-onset time), resulting in a positive shift of cross-correlation lag (middle). If cluster activity is response-associated, maximal cross-correlation will be centered on target onset, resulting in a zero shift across all RT bins (right). Fastest bin- magenta; slowest bin– yellow. ***(B)-(E)*** *Cross-correlogram of response-locked neural activity at different RT bins (pink- fastest RT; yellow - slowest RT) as a function of cross-correlation lag (left columns), and Pearson correlation (grey line) between maximal cross-correlation lags (Max lag) and bin's mean target onsets (right columns), across the 8 conditions (Congruent / Incongruent X short-SOA / long-SOA X Ipsilateral target / contralateral target) for RT-Cluster 1 (yellow), RT- Cluster 2a (orange), RT- Cluster 2b (turquoise) and RT- Cluster 3 (green).* ***(B)-(C)*** *Activity in RT-Cluster 1 & RT-Cluster 2a is target-associated: Cross-correlation plots are positively shifted in a spatially sensitive manner, i.e. only for contralateral targets.* ***(D)-(E)****. Activity in RT-Cluster 2b & RT-Cluster 3 is response-associated: Cross-correlation plots show no shift.* ***(F)*** *Significant positive correlation between cross-correlation maximal lag and bin mean RT in the RT-Cluster 1 & RT-Cluster 2a: significant (p<0.05) positive correlations were found mainly in these two clusters, only for contralateral targets.*

Finally, we examined the spatiotemporal relationships between the clusters. The three target-locked clusters formed a temporal gradient (Fig. 4A-B). The earliest activity emerged at Cluster 1, which peaked around 182±78ms post-target. Then followed Cluster 2 (262±75ms post-target), and finally Cluster 3 (383±141ms post-target; Mixed Anova: Cluster main effect $F(2,229)=102.7$, $p<0.001$, $\eta^2=0.378$; linear polynomial contrast: $p\leq0.001$).

We then examined the spatial relationships between the clusters and explored how it relates to the cortical gradient (Huntenburg et al., 2018). The position of a region along the gradient reflects its anatomical and functional cortical features (Gao et al., 2020; Huntenburg et al., 2018), and can be described using a 2-dimensional coordinate system that represents location along the early sensory and motor Periphery to the high-level multisensory Core (Margulies et al., 2016). Two main components define this 2-dimensional coordinate system: Dimension 1 extends from primary unimodal to transmodal regions, and Dimension 2 separates somatomotor and auditory cortices from visual cortex (Margulies et al., 2016). Cluster 1 contacts were the most peripheral and closest to the visual end of Dimension 2; contacts in the Cluster 3 were the closest to the core, extending from the somatomotor end to transmodal regions (Dimension 1 electrode values: 1-way Anova: $F(2,229)=7.74$; $p<0.001$, $\eta^2=0.06$; linear polynomial contrast: $p\leq0.001$; Dimension 2 electrode values: 1-way Anova: $F(2,229)=77.79$; $p<0.001$, $\eta^2=0.28$; linear polynomial contrast: $p\leq0.001$; Fig. 4C-D). A similar spatiotemporal gradient emerged in the response-locked clusters (Fig. 4E-H). Notably, locking activity to the response allowed separating the peripheral RT-Cluster 2a contacts from the RT-Cluster 2b contacts, which were closer to the core (Fig. S10). Thus, both target-locked and response-locked clusters mapped onto the cortical gradient topography.

Importantly, one of the features that changes along the cortical gradient is the length of temporal receptive windows (TRW, i.e. the time window in which previously presented information can affect the processing of a newly arriving stimulus), which lengthen and integrate over longer durations when moving up the gradient (Gao et al., 2020; Hasson et al., 2008; Huntenburg et al., 2018; Murray et al., 2014). Therefore, we asked if TRWs also lengthen along the cluster gradient because it is embedded in the cortical gradient and thus shares similar hierarchical characteristics. We estimated TRW length by calculating the decay time constant of the autocorrelation function applied to the non-filtered neural time series for each contact in the three clusters (Honey et al., 2012; Murray et al., 2014). TRW length increased when moving up the cluster gradient (Fig. 4E; TRW length: Cluster 1 to 54.33±44.96; Cluster 2 to 102.56±99.15; Cluster 3 to 124.91±87.13; 1-way Anova: $F(2,103.98)=17.83$; $p<0.001$, $\eta^2=0.113$; linear polynomial contrast: $p\leq0.001$), suggesting that along this trajectory, integration is over longer durations (Himberger et al., 2018; Huntenburg et al., 2018; Kiebel et al., 2008).

Lastly, we asked if the contacts within each cluster are structurally connected. We divided each cluster's contacts into pre rolandic contacts, located in the occipital, parietal and temporal lobes, and post roladic contacts, located in the frontal lobe, using the central sulcus as a landmark. A fiber tracking analysis paired with probability maps in 176 healthy individuals from the Human Connectome Project database (Vu et al., 2015) revealed that white matter tracts significantly connected pre-rolandic and post-rolandic contacts in the three clusters, suggesting these clusters' long-range contacts formed structural networks (Fig. 4F; threshold-free cluster enhancement-based non-parametric t-test, $p<0.05$). We then examined the overlap of the connecting pre and post rolandic fibers with the three branches of the superior longitudinal fasciculus (SLF I; SLF II; SLF II), which connect the ventral and dorsal attention networks (Bartolomeo et al., 2012; Corbetta and Shulman, 2002; Thiebaut de Schotten et al., 2005, 2011). A probability cut-off of 50% was used for the SLF maps and the resulting overlap was normalized to the number of cluster contacts per hemisphere. In Cluster 1, the connecting tracts mainly overlapped with SLF II in both hemispheres (Left hemisphere: SLF II 76.98%, SLF I 22.31%, SLF III 7.22%; Right hemisphere: SLF II 96.80%, SLF I 23.03%, SLF III 2.56%). In the right hemisphere of the right-lateralized Cluster 2 there was a major overlap with SLF II, a smaller overlap with SLF III, and a minimal overlap with SLF I (SLF II 45.67%; SLF III 23.80%; SLF I 3.05%). An opposite pattern was found in the left hemisphere, where tracts overlapped with SLF III and had a smaller overlap with SLF II (SLF III 43.35%, SLF II 35.11%, SLF I 0.03%). In the left-lateralized Cluster 3, connecting tract in the left hemisphere overlapped mainly with SLF III and had a small overlap with SLF II and a minimal overlap with SLF I (SLF III 36.78%; SLF II 28.45%; SLF I 0.65%). In the right hemisphere, Cluster 3 fibers were mainly associated with the SLF II and only minimally overlapped with SLF III and SLF I (SLF II 53.66%; SLF III 4.96%; SLF I 9.50%). These findings suggest that the functional clusters correspond to well-defined anatomical networks.

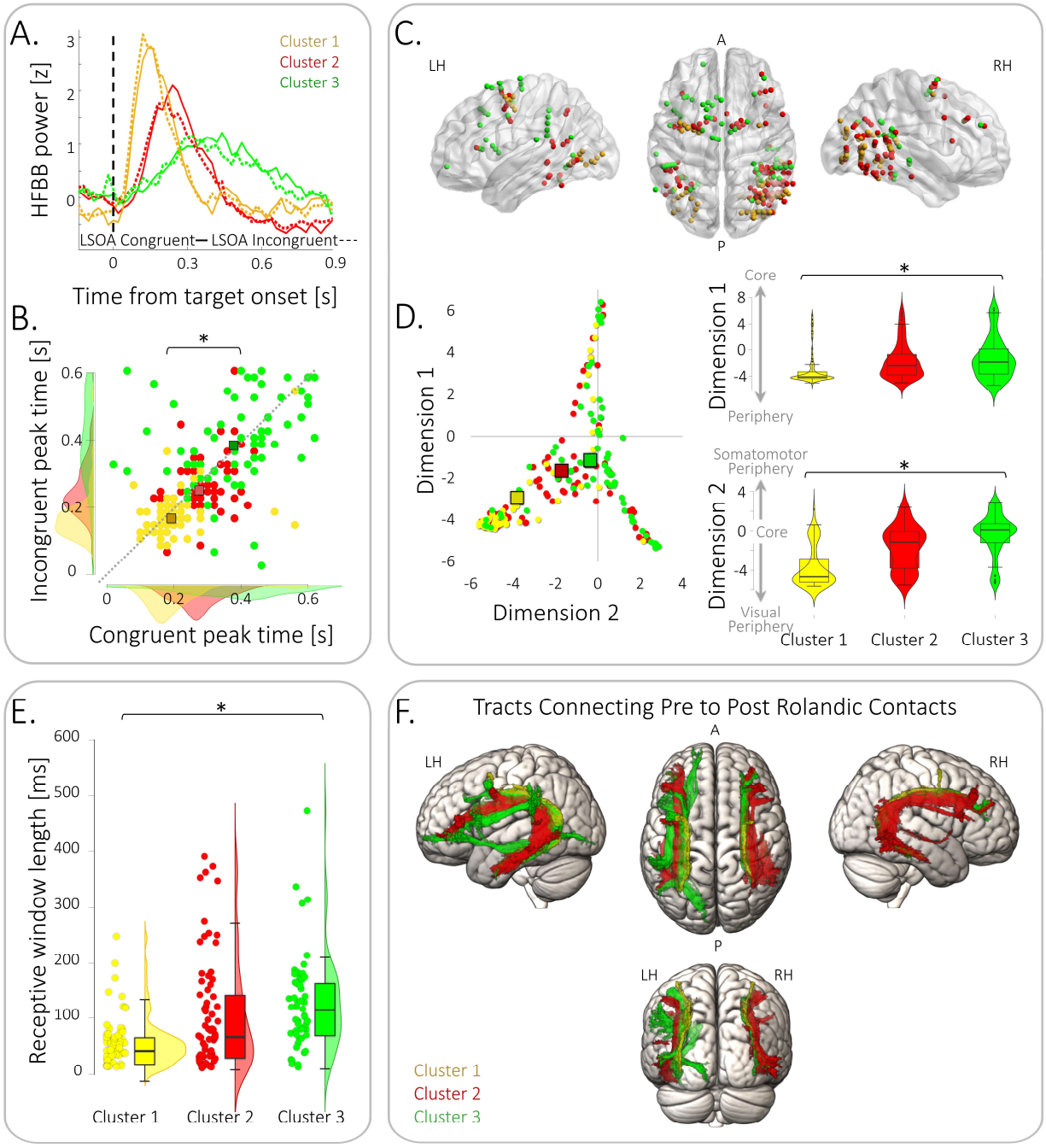

Figure 4 – Clusters exhibit a spatiotemporal gradient. ***(A)*** *Temporal gradient of activity in target-locked clusters: Trimmed-mean target-locked response of the Cluster 1, Middle and Cluster 3s. Black dashed line depicts target onset.* ***(B)*** *Scatter plot of peak times of mean target-locked activity of the contacts of the Early (yellow circles), the Middle (red circles) and the Late (green circles) clusters, in the Congruent (x axis) and Incongruent (y-axis) conditions, showing a significant temporal gradient ($p<0.001$, $\eta^2=0.378$; linear polynomial contrast: $p\leq0.001$). Squares represent mean peak time; Dotted grey line denotes the equity line; Shaded areas represent peak time distributions.* ***(C)*** *Core-Periphery gradient: Clusters' anatomical localization follows Core-Periphery gradients* (Margulies et al., 2016)*, where the Cluster 1's contacts are the most peripheral and the Cluster 3's contacts are closest to core regions.* ***(D)*** *Left: Scatter plot of contacts localization along core-periphery gradients (Cluster 1 - yellow circles; Cluster 2 - red circles; Late – green circles; rectangles represent clusters' mean). Right: Violin plots of contacts localization along Core-Periphery gradients for Cluster 1 (yellow), Cluster 2 (red) and Cluster 3 (green), showing a significant core-periphery gradient (Gradient 1: $p<0.001$,*

η^2=0.06; linear polynomial contrast: p≤0.001; Gradient 2: p<0.001, η^2=0.28; linear polynomial contrast: p≤0.001). ***(E)*** *Contacts' receptive windows lengthen along the cluster gradient: Raincloud plots of individual contacts' receptive window length (circles), showing a significant linear lengthening from Cluster 1 (yellow), to Cluster 2 (red), to Cluster 3 (green; p<0.001, η^2=0.11; linear polynomial contrast: p≤0.001).* ***(F)*** *Cluster contacts are structurally connected: Corrected tractography t-maps, showing the significant white matter voxels, which connect pre and post rolandic contacts within each cluster (Cluster 1 – yellow; Cluster 2 - red, Cluster 3 - green), derived from a fiber tracking analysis of 176 healthy individuals.*

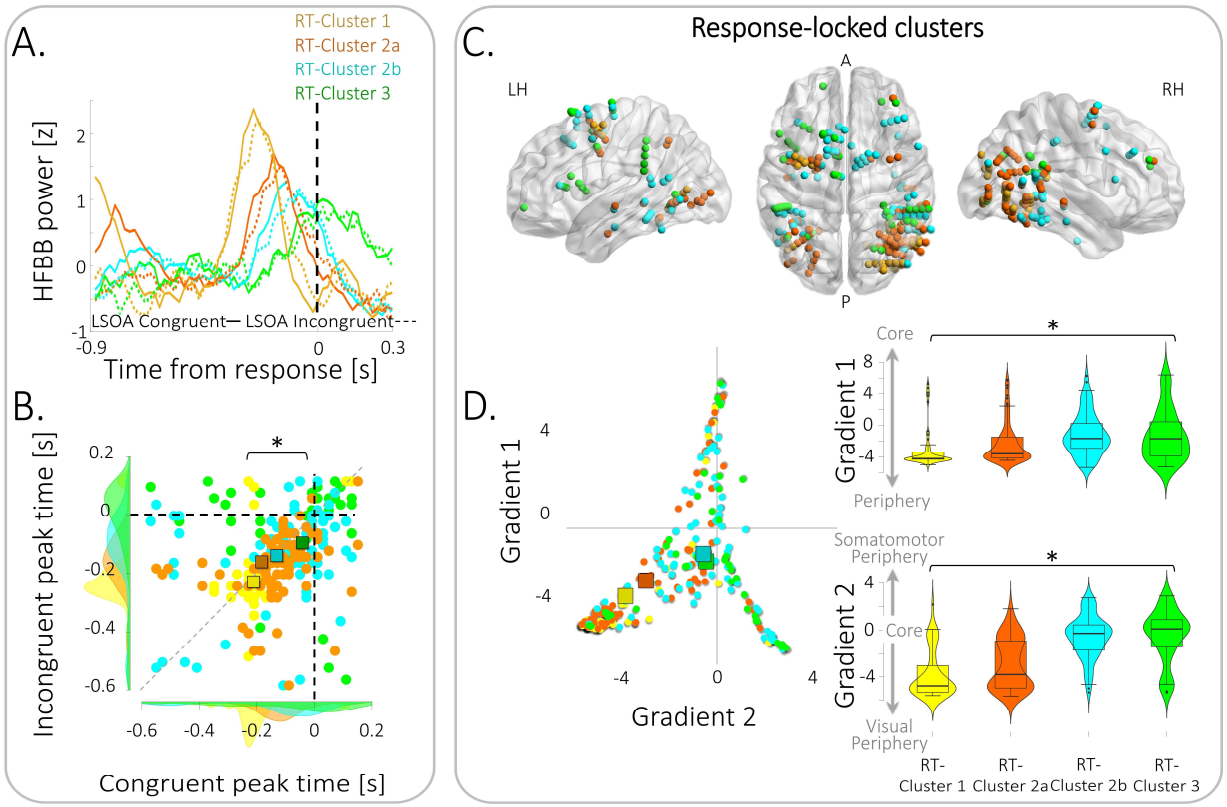

Figure S10 *– Response-locked clusters exhibit a spatiotemporal gradient.* ***A.*** *Temporal gradient of activity in response-locked clusters: Trimmed-mean response-locked response of the RT-Cluster 1, RT-Cluster 2a, RT-Cluster 2b and Cluster 3. Black dashed line depicts RT.* ***B.*** *Scatter plot of peak times of mean response-locked activity of the contacts of RT-Cluster 1 (yellow circles), RT-Cluster 2a (orange circles), RT-Cluster 2b (turquoise circles) and RT-Cluster 3 (green circles) clusters, in the Congruent (x axis) and Incongruent (y-axis) long-SOA conditions, showing a significant temporal gradient (Mixed Anova: Cluster main effect F(3,245)=12.57, p<0.001, η^2=0.086; linear polynomial contrast: p≤0.001). Squares represent mean peak time; Dotted grey line denotes the equity line; Shaded areas represent peak time distributions.* ***C.*** *Core-Periphery gradient: Clusters' anatomical localization follows Core-Periphery gradients (Margulies et al., 2016), where RT-Cluster 1's contacts are the most peripheral and RT-Cluster 3's contacts are closest to core regions.* ***D.*** *Left: Scatter plot of contacts localization along core-periphery gradients (RT-Cluster 1 - yellow circles; RT-Cluster 2a - orange circles; RT-Cluster 2b – turquoise circles; RT-Cluster 3 - green circles). Top & bottom right: Violin plots of contacts localization along Core-Periphery gradients for RT-Cluster 1 (yellow), RT-Cluster 2a (orange), RT-Cluster 2b (turquoise) and RT-Cluster 3 (green) clusters, showing a significant core-periphery gradient (Gradient 1: p=0.001, η^2=0.06; linear polynomial contrast: p≤0.001; Gradient 2: p<0.001, η^2=0.32; linear polynomial contrast: p≤0.001).*

Discussion

Here we aimed to establish how attention-capturing events modulate visual, attentional and response-associated neural processing in the human brain, and how the involved brain networks map onto the large-scale cortical topography. Overall, we provide a high-resolution, comprehensive depiction of the cortical dynamics underlying human exogenous attention. Our findings reveal that attentional events differentially define neural activity along a series of clusters, which form a spatiotemporal gradient, extending from the

visual cortex to frontoparietal regions. This gradient is embedded in the periphery-core cortical topography, which is a primary organizing axis of the human cerebral cortex (Huntenburg et al., 2018; Margulies et al., 2016; Mesulam, 2000). Cluster neural activity at one end of the gradient is modulated by visual attributes, while activity at the gradient's other end reflect the timing of the upcoming response, with attentional modulations occurring at the intersection of visual and response signals. Notably, temporally-close stimuli elicit discrete neural responses at the visual end of the gradient, yet at its frontoparietal end, they elicit a single pooled neural response. Moreover, TRW lengthen along the cluster gradient, like the hierarchy of timescales along the cortical topography in which the clusters are embedded. These findings stress the importance of studying fast and dynamic cognitive processes with high-resolution methods, and suggest that attention is not a discrete multi-step operation, but rather arises over large neural gradients embedded in the cortical topography, along which perceptual and response-related signals integrate.

We identified three key components along exogenous attention's cortical gradient. The first, Cluster 1, is situated at the peripheral end of the cortical gradient, encompassing the occipito-temporal cortex (Rosenke et al., 2021), and the vicinity of the FEFs (Vernet et al., 2014), where ultra-fast visual activation was reported (Kirchner et al., 2009). Its occipital and FEF-adjacent contacts were structurally connected mainly by the middle branch of the SLF (SLF II). Functionally, it only responded to contralateral visual stimuli, and its neural responses to the cue and target were segregated, even at the short cue-target delay.

Clusters 2 and 3 are located closer to core regions of the cortical gradient, and overlap with known frontoparietal attention networks (Buschman and Kastner, 2015; Corbetta and Shulman, 2002; Helfrich et al., 2018). The neural activity in Cluster 2, occurring midway along the gradient, is sensitive to cue-target spatial positions and delays, and exhibits IOR-related onset and offset. Both visual processing of the target and manual response preparation shape the neural activity in this cluster, which is lateralized to the right hemisphere, consistent with lesion and neurostimulation data on IOR (Bourgeois et al., 2012, 2013a, 2013b; Ro et al., 2003; Siéroff et al., 2007). Our results suggest that this cluster's activity represents a key attentional processing, associating perception and action signals.

On the other hand, neural activity in Cluster 3 shows sensitivity to stimulus identity, with stronger activation for response-requiring targets than for cues. It is lateralized to the left hemisphere, contralateral to the responding hand, and its response-locked activity peaks at the time of the motor response, which also modulates its target-locked activity. Furthermore, this cluster is anatomically situated between the somatomotor end and transmodal core regions of the core-periphery gradients. Therefore, Cluster 3 may encode decisional and motor aspects.

Along all this gradient of clusters, neural activity shows spatial sensitivity, sensitivity to cue-target delay, sensitivity to task relevance, and association with RT, therefore encoding the information necessary to underlie exogenous attention RT effects such as IOR, which depend on the delay and co-localization of attentional events.

Importantly, these findings depart from traditional attention models of multi-step processing across visual areas. Instead, exogenous attentional effects seem to emerges along a continuous neural trajectory of large-scale cortical gradient, that bridges perceptual and response processing. These findings reconcile long debated theories about the perceptual-motor (or input-output) dichotomy of attentional processes (Lupiáñez et al., 2006; Martín-Arévalo et al., 2016; Taylor and Klein, 2000). We find both perceptual and motor effects; however, they form a gradient rather than a dichotomy. These findings dovetail the idea

that attention organizes the activity of sensory and motor networks, generating alternating states for sampling sensory information versus shifting attention and responding (Fiebelkorn and Kastner, 2019).

Despite the overlap of Clusters 2 and 3 with known frontoparietal attention networks, their anatomy and function diverge from neurophysiological models of human attention (e.g. Corbetta and Shulman, 2002). First, in the TPJ, which constitutes a single node of the right-lateralized ventral attention network (Corbetta and Shulman, 2002), these clusters occupy distinct portions, which differ in their functional and structural connectivity (Bartolomeo and Seidel Malkinson, 2019; Hattori et al., 2018; Mars et al., 2012; Thiebaut de Schotten et al., 2011). The caudal TPJ portion (Cluster 2) connects to the superior frontal gyrus/FEF of the dorsal attention network (Bartolomeo and Seidel Malkinson, 2019; Hattori et al., 2018; Thiebaut de Schotten et al., 2011) through the middle branch of the SLF (SLF II), and thus provides direct communication between the ventral and dorsal attention networks.

In contrast, the rostral TPJ (Cluster 3) is connected to the middle and inferior frontal gyri through the ventral branch of the SLF (SLF III), thus linking nodes of the ventral attention network. Both SLF II and SLF III show anatomical or functional lateralization to the right hemisphere (Thiebaut de Schotten et al., 2011) and their inactivation or disconnection was associated with signs of left spatial neglect (Bourgeois et al., 2012; Thiebaut de Schotten et al., 2005). Indeed, our findings demonstrate that temporo-parietal and prefrontal contacts in Clusters 2 and 3 are connected by the SLF, and our overlap analysis suggests that in the right hemisphere the right-lateralized Cluster 2 is more connected by the SLF II, while the left-lateralized Cluster 3 is more connected by the SLF III in the left hemisphere. Yet because of the overlap between probabilistic maps of SLF II and III templates, these latter findings should be validated in future studies, exploring neural activity and tractography in the same sample of participants.

Similarly, Clusters 1, 2 and 3 encompass contacts in the dorsolateral prefrontal cortex, indicating that when examining in sufficient spatiotemporal resolution, this region, which constitutes a single node of the dorsal attention network (Corbetta and Shulman, 2002), can be dissociated into distinct networks.

Furthermore, our findings localizing contacts from Cluster 2 and 3 to the posterior temporal lobe, a region outside the scope of hallmark attention models (Buschman and Kastner, 2015; Corbetta and Shulman, 2002), suggest that this area may contribute to exogenous attention processing, dovetailing recent studies in humans and non-human primates (Sani et al., 2021; Stemmann and Freiwald, 2019).

Functionally, our findings suggest that contrary to the stipulations of these models, not only do the prefrontal nodes of the dorsal attention network process information pertaining to the contralateral visual field (Bartolomeo and Seidel Malkinson, 2019; Szczepanski and Kastner, 2013), but rather respond to stimuli in both contralateral and ipsilateral visual fields. Conversely, the activity recorded in contacts in the TPJ belonging to Cluster 2 presented spatial sensitivity, contrary to assumption of some models that this functional region lacks spatial mapping (Corbetta and Shulman, 2002). Additionally, TPJ contacts were activated also in response to cues, and in congruent trials, when target location corresponded to the location of the preceding cue, therefore suggesting that the TPJ is not just a circuit breaker responding when unexpected and pertinent targets appear and reorienting of attention is needed (Corbetta and Shulman, 2002).

What are the cortical characteristics that favor the localization of attentional processing to a particular extent of the cluster gradient? Beside the convergence of perceptual and response signals, a potential factor might be the temporal integration properties of the involved regions. This trait changes in a

continuous manner along the temporal hierarchy of TRWs, a key feature of the core-periphery gradient, analogous to the spatial hierarchy of receptive fields (Gao et al., 2020; Hasson et al., 2008; Himberger et al., 2018; Huntenburg et al., 2018; Kiebel et al., 2008; Stigliani et al., 2017; Zhou et al., 2018). TRWs lengthen as we move from unimodal regions (e.g., early visual cortex), to association regions (e.g., the intraparietal sulcus). Thus, along this trajectory, integration is over longer durations, and selectivity for coherent temporal structures increases (Hasson et al., 2008; Himberger et al., 2018; Huntenburg et al., 2018; Kiebel et al., 2008). TRW length is an intrinsic property of a region, defined by its cortical variations in cytoarchitecture, as well as both macroscale and microcircuit connectivity (Gao et al., 2020; Kiebel et al., 2008). Such hierarchy of temporal scales could enable a dynamical interaction with a continuously changing environment, with fast fluctuations associated with sensory processing at the bottom of the hierarchy, and slow fluctuations, which reflect contextual changes in the environment, at the hierarchy top (Kiebel et al., 2008). Moreover, a hierarchy of TRWs can serve as a scaffold for putative recurrent temporal computations that support neuronal sensitivity to sequential events, and boost robustness to changes in input gain and timing, such as temporal pooling, i.e. the integration of prior information across the temporal window (Himberger et al., 2018). Indeed, recent evidence showed that neural timescales could serve cognitive functions (Gao et al., 2020; Kim and Sejnowski, 2021; Wasmuht et al., 2018). For example, prefrontal cortex timescales expanded during working memory maintenance and predicted individual performance (Gao et al., 2020). Correspondingly, our finding that TRWs lengthen along the cluster gradient reveal potential temporal operations at the basis of exogenous attention. Furthermore, the integration of cue-target responses in Clusters 2 and 3 in the long-SOA could reflect temporal pooling (Himberger et al., 2018). In Cluster 1, situated lower on the gradient, temporal receptive windows are shorter, allowing for segregation of activity even at short delays. In upstream frontoparietal clusters where temporal windows are longer, cue- and target-induced responses resulted in a single activity peak. This temporal pooling might group the cue and target in a single event (Krüger et al., 2014), leading to *RT facilitation* at short cue-target delays (Krüger et al., 2014; Lupiáñez, 2010; Seidel Malkinson and Bartolomeo, 2018). These findings dovetail with the hypothesis that *RT facilitation* results from a summation of cue-related and target-related responses, thus reflecting hard-wired limitations of the neural system that cannot respond separately to rapidly repeated stimuli, and processes them as a single event (Krüger et al., 2014; Lupiáñez, 2010; Seidel Malkinson and Bartolomeo, 2018). Longer cue-target delays could instead provide the system with enough time to segregate cue- and target-related responses (Lupiáñez, 2010; Seidel Malkinson and Bartolomeo, 2018). As for the phenomenon of IOR, our findings suggest that in Cluster 2, the timing of response peak and decay may be involved in the generation of IOR, but whether or not these dynamics relate to temporal operations will be investigated in the future. Thus, our study contributes to the understanding of the temporal mechanisms involved in cognitive processes.

iEEG provides robust signals with unparalleled spatiotemporal resolution in humans, but it also has limitations (Lachaux et al., 2003; Mukamel and Fried, 2012; Parvizi and Kastner, 2018). Although contacts with epileptic activity are discarded from the analysis, iEEG data is collected from a pathological population, which might not be a valid model for neurotypical cognition. However, the fact that our participants demonstrated a neurotypical pattern of behavioral responses is reassuring in this respect. In addition, iEEG has a limited and inhomogeneous spatial coverage, determined solely by medical needs. We mitigated this limitation by collecting a large set of data from 28 patients thus achieving a comprehensive coverage, and by taking the coverage into account in our analyses when needed, i.e. when comparing cluster hemispheric lateralization. As a result, some parts of the puzzle might be missing, yet the high signal-to-noise ratio and the excellent resolution in the covered regions ensure that the activity recorded form them is robust.

Our findings support a model of time-resolved segregation and integration of attentional events as a large-scale brain process within the context of the general topography of the cortex. These neural dynamics are a potential mechanism through which the timing of attentional events shapes neural processing and consequently our behavior. Our findings suggest that the circuits for attention form a dynamic network, in which attentional effects are properties of the overall network, not separate functions assigned to different parts (Krauzlis et al., 2021), placing exogenous attention processing in the context of the larger topographical organization of the human brain.

STAR Methods

Participants and recordings

Thirty one patients (aged 31.8 ± 8.3 years, 16 women; See Table 1 for full details) with drug-resistant focal epilepsy, hospitalized at the Pitié-Salpêtrière Hospital in Paris, participated in this study after giving their informed consent (CPP Paris VI, Pitié-Salpêtrière Hospital, INSERM C11-16). Three patients were excluded post hoc because of severe cognitive impairments and abnormally long response times (1 patient) or because of the presence of wide-spread brain lesions (2 patients), leaving a total of 28 included patients. For medical reasons, patients underwent intracerebral recordings by means of stereotactically implanted, multilead intracerebral depth electrodes (iEEG). Patients were implanted with 5–12 platinum electrodes (AdTech®, Wisconsin) endowed with 4-12 contacts with a diameter of 1.12 mm and length of 2.41 mm, with nickel-chromium wiring. The distance between the centers of two contacts is 5 mm. Electrode placement was uniquely determined by clinical criteria. In 13 patients neuronal recordings were performed using an audio–video–EEG monitoring system (Micromed), which allowed simultaneous recording of 128 depth-EEG channels sampled at 1024 Hz (0.18 to 220 Hz bandwidth). In 18 patients the recording was done with a Neuralynx system (ATLAS, Neuralynx, Inc.), allowing to record up to 160 depth-EEG channels sampled at 4 KHz (0.1 to 1000 Hz bandwidth). The least active electrode (preferably in white matter) was defined as the reference electrode. Before analysis, all signals were down sampled to 512Hz and re-referenced to their nearest neighbor on the same electrode, yielding a bipolar montage. Bipolar montage helps eliminating signal artifacts common to adjacent electrode contacts (such as 50Hz line artifact) and achieves a high local specificity by cancelling out effects of distant sources that spread equally to both adjacent sites through volume conduction.

Spatial localization of the electrode was automatically computed in native space using the Epiloc toolbox (Pérez-García et al., 2015) developed by the STIM engineering facility at the Paris Brain Institute (https://icm-institute.org/fen/cenir-stim//) using co-registered pre-implantation 1.5T or 3T MR scans and post-implantation CT scans. Each contact localization was automatically labeled according to the Desikan-Killiany-Tourville atlas parcellation (Desikan et al., 2006) in patients' native space, using Freesurfer image analysis suite (http://surfer.nmr.mgh.harvard.edu/) that is embedded in Epiloc. In 10 participants with low quality MRI scans for which automatic contact labelling was not possible, two experimenters labeled manually and independently the contacts (inter-rater reliability R=0.99) based on anatomical landmarks in the patients' native space, according to the parcellation of the Desikan-Killiany-Tourville atlas (Desikan et al., 2006).

Experimental task

A PC Dell Latitude D600 running E-prime 3.0 software (Psychology Software Tools, Pittsburgh, PA) controlled the presentation of stimuli, timing operations, and data collection. Stimuli were presented on a black background. Two grey empty boxes (3° long and 2.5° large) were horizontally arranged around a

central fixation point, located at the center of the screen. The distance between the center of the fixation point and the center of each box was 7.7°. The fixation point consisted of a grey plus sign (0.5° x 0.5°). Cues consisted of a 100-ms thickening (from 1 mm to 3 mm) of the contour of one lateral box. The target was a white "X" (1° in height), appearing at the center of one of the lateral boxes, with equal probability. Patients sat in front of the computer screen at a distance of approximately 57 cm. Fig. 1A illustrates the experimental procedure. Each trial began with the appearance of the fixation point and the two placeholder boxes for 1,000 ms. The cue followed for a duration of 100 ms. After a stimulus-onset asynchrony (SOA) of either 150 ms or 600 ms, the target appeared and remained visible for 150 ms. The placeholder boxes disappeared when a response was detected or after 3000 ms if no response was made. The experiment consisted of a total of 3 blocks of 112 trials, comprising 50 short SOA trials, 50 long SOA trials, and 12 catch trials, in which no target appeared after the cue, all randomly interleaved. Cues were non-informative, i.e. they indicated the target location on 50% of trials (Congruent location), and the opposite location (Incongruent location) on the remaining 50% of the trials. Patients were instructed to maintain their gaze at the central fixation point throughout the test, and to respond to the target as fast and accurately as possible, by pressing the right mouse button with their right index finger. Gaze position was verified by confrontation. The mouse was placed in an approximately central position with respect to the patient's body midline. It was stressed that the position of cues was useless for predicting the target position, and should not be taken into account when responding. Before the first experimental block, patients performed 10 practice trials.

Behavioral analysis

For each participant, trials with response time (RT) exceeding 3 std or faster than 100 ms were excluded from analysis. Participants' mean RT were compared using a 2-way repeated measures ANOVA, with Congruence and SOA as factors, using JASP software (version 0.14.1) (Team, Jasp, 2020). All post hoc comparisons were corrected for multiple comparisons using the Holm correction.

iEEG preprocessing

Data preprocessing was done using FieldTrip toolbox for EEG/MEG-analysis (Donders Institute for Brain, Cognition and Behaviour, Radboud University, the Netherlands. See http://fieldtriptoolbox.org (Oostenveld et al., 2011)) and Matlab (Matlab R2016b and R2020a, The MathWorks, Inc.). Continuous iEEG signals were visually inspected. Electrodes with excessive epileptic spikes, located at or near the epileptic focus, were rejected. Then, time windows showing epileptic transient activity were identified and excluded from further analysis. Next, epochs were extracted, between 1 s before target onset and 1.5 s after target onset. Additionally, epochs were extracted, between 1 s before the response time and 0.4 s after it. A second artefact rejection procedure was then performed on the epoched data, and trials with excessive variance, maximal signal or kurtosis of their signal distribution were semi-automatically rejected. After epileptic artifact removal, 1403 of the bipolar contacts were usable for analysis, 671 of them were in the left hemisphere and 732 in the right hemisphere (see Fig. 1C and Table 2 for the localization of the usable contacts). According to the Desikan-Killiany-Tourville atlas parcellation (Desikan et al., 2006), 336 (23.9%) of the contacts were located in the frontal lobe, 689 (49.1%) in the temporal lobe, 48 (3.4%) in the occipital lobe, 138 (9.8%) in the parietal lobe, 46 (3.2%) in subcortical regions and 146 (10.4%) in white matter.

A pseudo-whole-brain analysis approach was selected, focusing on high-frequency broadband (HFBB) activity (55–145 Hz a-priori range), a marker for multi-unit neural activity (Ray and Maunsell, 2011), which was associated with various cognitive processes (Helfrich and Knight, 2019; Helfrich et al., 2018; Jensen et al., 2007). HFBB power was extracted from each bipolar contact time series, by convolving the signal with a set of complex Morlet wavelets (with 8 cycles), in 20 logarithmically spaced center frequency bands. Every

trace was separately baseline-corrected by means of a z-score relative to a the trials' baseline distribution in the 700 ms prior to cue onset, separately for each of the frequency bands. This approach accounts for the 1/f signal drop off in the high-frequency band with increasing frequencies. Finally, we discarded the edges to avoid filter artifacts and extracted individual non-overlapping trials relative to either target onset (−0.9 to 1.36 s) or relative to the response time (−0.9 to 0.3 s). HFBB signals were down-sampled to 50 Hz for further analysis.

Trajectory k-means clustering

In order to reveal contacts' prototypical temporal patterns of activity across experimental conditions, we developed a novel clustering approach based on k-means clustering, implemented through Matlab (Matlab R2016b and R2020a, The MathWorks, Inc.). Clustering was done on responsive contacts, defined as having a target-locked significant effect ($p \leq 0.05$ uncorrected) of at least 100 ms in one or more of the eight experimental conditions compared to baseline. For each condition in a given contact, a time resolved independent samples t-test was performed, in which each time point across trials was compared to the distribution of all the baseline samples pooled over all that condition's trials (-0.2-0 s prior to cue onset). This yielded 644 contacts (See Table 2 for their spatial localization), for which the trajectories of the mean target-locked or response-locked activity across the 8-dimensional condition space were entered into the clustering algorithm. Activity across conditions was z-scored relative to the distribution of the trials' entire duration. Trajectories were iteratively partitioned (10000 iterations) into 2-9 clusters, in which each contact was assigned to the cluster with the nearest centroid trajectory. This was achieved by minimizing the sum of the Manhattan distances, time-point-by-time point to quantify trajectories similarity while preserving temporal order. Based on the elbow method (Kodinariya and Makwana, 2013) the 6-cluster solution was chosen for the clustering of target-locked activity (See Fig. S2), and for the clustering of response-locked activity a 7-cluster solution was chosen (See Fig. S4). In order to identify the correspondence between target-locked and response-locked clusters, a contingency analysis was performed using JASP (Team, Jasp, 2020). Figure S6 shows the clustering of target-locked activity for 2-8 cluster solutions, demonstrating the stability of the three clusters further analyzed across solutions. The distribution of the 28 participants' contacts across target-locked and response-locked clusters is shown in Fig. S7, demonstrating that clusters did not result from any single participant's temporal activity, but rather reflected temporal patterns across many participants. The linear correlation between the centroid time-series of all conditions across target-locked clusters revealed that out of the six target-locked clusters, three had a dynamic temporal profile across the different experimental conditions. These clusters were positively correlated among themselves, forming a distinct cluster group (See Fig. S8). These clusters were used as a type of functional region of interest for further analyses. The correlation pattern within the remaining three clusters was more uniform, and negatively correlated across clusters.

Clusters hemispheric lateralization

The hemispheric lateralization of the clusters was tested on a subgroup of contacts localized in cortical volumes that were sampled in both hemispheres. This was done to overcome the confound of unequal coverage within the hemispheres. To identify similarly-covered contacts, a 3 mm radius sphere (corresponding to the assumed volume recorded by iEEG contacts (Mukamel and Fried, 2012)) was fit around each contact using SPM12 (Friston et al., 2010), and the overlap between each of the spheres and the entire covered volume in the other hemisphere was calculated. The cluster-distribution of the 309 resulting contacts (148 in the left hemisphere and 161 in the right hemisphere) across the hemispheres

was compared using a contingency analysis in JASP (Team, Jasp, 2020), and post hoc binomial test with holm correction were conducted to identify the clusters with significant hemispheric lateralization.

iEEG statistical analyses

All statistical analyses were performed using statistical toolbox in Matlab (Matlab, R2020a, The MathWorks, Inc.) and JASP (Team, Jasp, 2020).

IOR-related neural activity

In order to test in which of the clusters neural activity was IOR-related, we compared between Congruent and Incongruent trials in the long SOA condition, For each cluster, we performed a time resolved 3-way ANOVA (Fig. 2) with Congruence, Contact's Hemisphere and Target Laterality (relative to the contact), on the target-locked HFBB signal in each time point (between 0-0.8 s post target onset), across all the cluster's trials (pooled over contacts and participants). Holm multiple comparisons correction was applied over all the time points within each main effect and interaction. Post hoc comparisons were performed on time points in which the Congruence*Hemisphere interaction was significant, with Holm correction for multiple comparisons. Detailed Anova corrected p-values for each cluster are shown in Table S1.

RT-modulation of target-locked neural activity and visual modulation of response-locked neural activity

In order to test in which of the clusters neural activity was modulated by the RT, we sorted in each cluster all the trials pooled over the conditions according to their RT. We then binned them into 20 quantiles (Fig. 3A). Within each cluster, we tested the effect of the RT-bin using a time-resolved 1-way repeated measures ANOVA, on mean target-locked HFBB signal across conditions, in each time point (between 0-0.8 s post target onset; pooled over contacts and participants). Holm multiple comparisons correction was applied over all the time points. Similar analysis was performed on the response-locked clusters. Because RT is defined as the time from target onset to the response, this procedure sorted the response-locked trials according to target onset, and thus could unveil visual modulation of response-locked activity.

Cross-correlation of target-locked and response-locked RT-bins

This analysis intended to explore the link between target-locked neural activity and RT. We sorted in each cluster all the trials pooled over the conditions according to their RT. We then binned them into 20 quantiles (Fig. S3A). In each cluster, a cross-correlation between target-locked activity at the fastest RT bin and all subsequent bins was computed for each experimental condition within a maximal lag of ±600 ms. If cluster activity is target-related, maximal cross-correlation will be centered on target onset, resulting in a zero shift across all RT bins. If cluster activity is response-modulated, maximal cross-correlation will follow the RT, resulting in a negative shift of cross-correlation lags. Next, in order to test whether the maximal lag corresponded to the actual RT (expecting significant negative correlation coefficients for RT-modulated activity), a Pearson correlation between the maximal cross-correlation lag and the each bin's mean RT was computed for each condition. Cross-correlation between response-locked activity at the fastest RT bin and all subsequent bins was similarly computed. Notably, if cluster response-locked activity is visually modulated, maximal cross-correlation will follow the RT (here marking quantile's mean target-onset time), resulting in a positive shift of the maximal cross-correlation lag. If cluster activity is only response-associated, maximal cross-correlation will be centered on target onset, resulting in a zero shift across all RT bins.

Temporal gradient analysis

Within each target-locked cluster, contacts' time of the maximal HFBB power (between 0-0.6s post target onset) was identified, separately for Congruent and Incongruent long SOA conditions. Contacts' peak times

were compared across the three clusters using a mixed-repeated measures ANOVA, with Congruence as a within subjects factor and Clusters as a between subjects factor. A linear post-hoc polynomial contrast was used to test if peak time was linearly ordered across clusters. Similar analysis was performed on the response-locked clusters.

Core-Periphery gradient analysis

In order to test if the clusters' anatomical localization followed the Core-Periphery gradients, the MNI coordinates of target-locked clusters' contacts were assigned the closest voxel's gradient value on the two principle gradients described by Margulies et al. (2016). The distances between contacts and the closest voxels did not differ across clusters (1-way ANOVA, $F_{(2,230)}$=0.064, p=0.94). Contacts' gradients' values along the two gradients were compared using a 1-way ANOVA with Clusters as a factor. A linear post-hoc polynomial contrast was used to test if clusters were linearly ordered along the two gradients. Similar analysis was performed on the response-locked clusters. Here too, the distances between contacts and the closest voxels did not differ across clusters (1-way ANOVA, $F_{(3,246)}$=1.23, p=0.30).

Estimation of temporal receptive window length

TRW length was assessed by computing the across-trial autocorrelation (Golesorkhi et al., 2020; Murray et al., 2014) of the non-filtered iEEG signal (down-sampled to 100Hz), for each of the contacts in the three target-locked clusters. An exponential decay function (e^(−t/τ)) was fit to the contacts autocorrelation coefficient across time-lags. TRW length for each contact was defined as the time constant (τ) of the contact's fitted exponential decay function, i.e., the time it takes for the autocorrelation to decrease by a factor of e (Golesorkhi et al., 2020; Murray et al., 2014).

Structural connectivity of pre and post rolandic contacts

To determine the connectional anatomy of the three clusters we used fiber tracking in a sample of 176 healthy controls from the Human Connectome Project database (Vu et al., 2015) and used a threshold-free cluster enhancement (TFCE)-based non-parametric t-test to determine the significant tracts. Contacts of each cluster were fitted with a 3mm radius sphere around them as described above, and labeled as pre or post rolandic, using the central sulcus as a reference point in patients native space (Number of pre and post rolandic contacts per cluster: Cluster 1 - 8:60, Cluster 2 - 23:74, Cluster 3 - 34:33). The resulting pre and post rolandic contact spheres were used as region-of-interests (ROIs) to identify white matter fibers connecting them. This fiber-tracking analysis was done on the high-resolution 7T MRI scans of 176 healthy individuals from the Human Connectome Project database (Vu et al., 2015) using TrackVis (http://trackvis.org/). The resulting tractography maps were binarized and significant tracts across individuals were determined using a threshold-free cluster enhancement (TFCE)-based non-parametric t-test in FSL (1000 permutations, height threshold of 0.95 to control significance level at p<0.05; https://fsl.fmrib.ox.ac.uk/fsl/fslwiki/FSL). The corrected t-maps were then used to identify the number of white matter voxels that overlapped with the SLF tracts templates of the white-matter probability maps of the BCBtoolkit (http://toolkit.bcblab.com/). In order to identify the tracks overlapping with the three branches of the SLF, probability maps were thresholded at 50%, yet the large overlap between the tracts of SLF II and SLF III templates (present even with a 90% probability threshold) made the differentiation between them difficult. The number of significant overlapping voxels between corrected t-maps and SLF maps was calculated per hemisphere. The corresponding voxels were then normalized for the number of significant voxels in the corrected t-maps [(Nr of overlapping voxels per SLF tract/ Nr of significant voxels in the corrected t-maps in the respective hemisphere)*100].

References

Anzola, G.P., Bertoloni, G., Buchtel, H.A., and Rizzolatti, G. (1977). Spatial compatibility and anatomical factors in simple and choice reaction time. Neuropsychologia *15*, 295–302.

Balan, P.F., and Gottlieb, J. (2006). Integration of exogenous input into a dynamic salience map revealed by perturbing attention. J. Neurosci. *26*, 9239–9249.

Bartolomeo, P., and Seidel Malkinson, T. (2019). Hemispheric lateralization of attention processes in the human brain. Curr Opin Psychol *29*, 90–96.

Bartolomeo, Thiebaut de Schotten, M., and Chica, A.B. (2012). Brain networks of visuospatial attention and their disruption in visual neglect. Front. Hum. Neurosci. *6*, 110.

Bourgeois, A., Chica, A.B., Migliaccio, R., Thiebaut de Schotten, M., and Bartolomeo, P. (2012). Cortical control of inhibition of return: evidence from patients with inferior parietal damage and visual neglect. Neuropsychologia *50*, 800–809.

Bourgeois, A., Chica, A.B., Valero-Cabre, A., and Bartolomeo, P. (2013a). Cortical control of inhibition of return: Causal evidence for task-dependent modulations by dorsal and ventral parietal regions. Cortex *49*, 2229–2238.

Bourgeois, A., Chica, A.B., Valero-Cabre, A., and Bartolomeo, P. (2013b). Cortical control of Inhibition of Return: Exploring the causal contributions of the left parietal cortex. Cortex *49*, 2927–2934.

Burrows, B.E., and Moore, T. (2009). Influence and limitations of popout in the selection of salient visual stimuli by area V4 neurons. J. Neurosci. *29*, 15169–15177.

Buschman, T.J., and Kastner, S. (2015). From Behavior to Neural Dynamics: An Integrated Theory of Attention. Neuron *88*, 127–144.

Buschman, T.J., and Miller, E.K. (2007). Top-down versus bottom-up control of attention in the prefrontal and posterior parietal cortices. Science *315*, 1860–1862.

Carrasco, M. (2011). Visual attention: the past 25 years. Vision Res. *51*, 1484–1525.

Chica, A.B., Martín-Arévalo, E., Botta, F., and Lupiánez, J. (2014). The Spatial Orienting paradigm: How to design and interpret spatial attention experiments. Neurosci. Biobehav. Rev. *40*, 35–51.

Corbetta, M., and Shulman, G.L. (2002). Control of goal-directed and stimulus-driven attention in the brain. Nat. Rev. Neurosci. *3*, 201–215.

Desikan, R.S., Ségonne, F., Fischl, B., Quinn, B.T., Dickerson, B.C., Blacker, D., Buckner, R.L., Dale, A.M., Maguire, R.P., Hyman, B.T., et al. (2006). An automated labeling system for subdividing the human cerebral cortex on MRI scans into gyral based regions of interest. Neuroimage *31*, 968–980.

Dorris, M.C., Klein, R.M., Everling, S., and Munoz, D.P. (2002). Contribution of the primate superior colliculus to inhibition of return. J. Cogn. Neurosci. *14*, 1256–1263.

Fiebelkorn, I.C., and Kastner, S. (2019). A Rhythmic Theory of Attention. Trends Cogn. Sci. *23*, 87–101.

Friston, K.J., Ashburner, J.T., Kiebel, S.J., Nichols, T.E., and Penny, W.D. (2010). Statistical parametric mapping: The analysis of functional brain images: The analysis of functional brain images (Academic Press).

Gabay, S., Leibovich, T., Ben-Simon, A., Henik, A., and Segev, R. (2013). Inhibition of return in the archer fish. Nat. Commun. *4*, 1657.

Gao, R., van den Brink, R.L., Pfeffer, T., and Voytek, B. (2020). Neuronal timescales are functionally dynamic and shaped by cortical microarchitecture. Elife *9*.

Goldberg, M.E., Bisley, J.W., Powell, K.D., and Gottlieb, J. (2006). Saccades, salience and attention: the role of the lateral intraparietal area in visual behavior. Prog. Brain Res. *155*, 157–175.

Golesorkhi, M., Tumati, S., Gomez-Pilar, J., Stamatakis, E.A., and Northoff, G. (2020). Time meets space – brain dynamics drive spatial topography.

Hasson, U., Yang, E., Vallines, I., Heeger, D.J., and Rubin, N. (2008). A hierarchy of temporal receptive windows in human cortex. J. Neurosci. *28*, 2539–2550.

Hattori, T., Ito, K., Nakazawa, C., Numasawa, Y., Watanabe, M., Aoki, S., Mizusawa, H., Ishiai, S., and Yokota, T. (2018). Structural connectivity in spatial attention network: reconstruction from left hemispatial neglect. Brain Imaging Behav. *12*, 309–323.

Hegdé, J., and Felleman, D.J. (2003). How selective are V1 cells for pop-out stimuli? J. Neurosci. *23*, 9968–9980.

Helfrich, R.F., and Knight, R.T. (2019). Chapter 3 - Cognitive neurophysiology of the prefrontal cortex. In Handbook of Clinical Neurology, M. D'Esposito, and J.H. Grafman, eds. (Elsevier), pp. 35–59.

Helfrich, R.F., Fiebelkorn, I.C., Szczepanski, S.M., Lin, J.J., Parvizi, J., Knight, R.T., and Kastner, S. (2018). Neural Mechanisms of Sustained Attention Are Rhythmic. Neuron *99*, 854-865.e5.

Himberger, K.D., Chien, H.-Y., and Honey, C.J. (2018). Principles of Temporal Processing Across the Cortical Hierarchy. Neuroscience *389*, 161–174.

Honey, C.J., Thesen, T., Donner, T.H., Silbert, L.J., Carlson, C.E., Devinsky, O., Doyle, W.K., Rubin, N., Heeger, D.J., and Hasson, U. (2012). Slow cortical dynamics and the accumulation of information over long timescales. Neuron *76*, 423–434.

Huntenburg, J.M., Bazin, P.-L., and Margulies, D.S. (2018). Large-Scale Gradients in Human Cortical Organization. Trends Cogn. Sci. *22*, 21–31.

Itti, L., and Koch, C. (2001). Computational modelling of visual attention. Nat. Rev. Neurosci. *2*, 194–203.

Jensen, O., Kaiser, J., and Lachaux, J.-P. (2007). Human gamma-frequency oscillations associated with attention and memory. Trends Neurosci. *30*, 317–324.

Kiebel, S.J., Daunizeau, J., and Friston, K.J. (2008). A hierarchy of time-scales and the brain. PLoS Comput. Biol. *4*, e1000209.

Kim, R., and Sejnowski, T.J. (2021). Strong inhibitory signaling underlies stable temporal dynamics and working memory in spiking neural networks. Nat. Neurosci. *24*, 129–139.

Kirchner, H., Barbeau, E.J., Thorpe, S.J., Régis, J., and Liégeois-Chauvel, C. (2009). Ultra-rapid sensory responses in the human frontal eye field region. J. Neurosci. *29*, 7599–7606.

Kodinariya, T.M., and Makwana, P.R. (2013). Review on determining number of Cluster in K-Means Clustering. Aquat. Microb. Ecol. *1*, 90–95.

Krauzlis, R.J., Wang, L., Yu, G., and Katz, L.N. (2021). What is attention? Wiley Interdiscip. Rev. Cogn. Sci. e1570.

Krüger, H.M., MacInnes, W.J., and Hunt, A.R. (2014). Perceptual merging contributes to cueing effects. J. Vis. *14*.

Lachaux, J.P., Rudrauf, D., and Kahane, P. (2003). Intracranial EEG and human brain mapping. J. Physiol. Paris *97*, 613–628.

Lev-Ari, T., Zahar, Y., Agarwal, A., and Gutfreund, Y. (2020). Behavioral and neuronal study of inhibition of return in barn owls. Sci. Rep. *10*, 7267.

Lupiáñez, J. (2010). Inhibition of return. In Attention and Time, A.C. Nobre, and J.T. Coulle, eds. (Oxford University Press), pp. 17–34.

Lupiáñez, J., Klein, R.M., and Bartolomeo, P. (2006). Inhibition of return: Twenty years after. Cogn. Neuropsychol. *23*, 1003–1014.

Lupiáñez, J., Martín-Arévalo, E., and Chica, A.B. (2013). Is Inhibition of Return due to attentional disengagement or to a detection cost? The Detection Cost Theory of IOR. Psicologica: International Journal of Methodology and Experimental Psychology *34*, 221–252.

Margulies, D.S., Ghosh, S.S., Goulas, A., Falkiewicz, M., Huntenburg, J.M., Langs, G., Bezgin, G., Eickhoff, S.B., Castellanos, F.X., Petrides, M., et al. (2016). Situating the default-mode network along a principal gradient of macroscale cortical organization. Proc. Natl. Acad. Sci. U. S. A. *113*, 12574–12579.

Mars, R.B., Sallet, J., Schüffelgen, U., Jbabdi, S., Toni, I., and Rushworth, M.F. (2012). Connectivity-based subdivisions of the human right "temporoparietal junction area": evidence for different areas participating in different cortical networks. Cereb. Cortex *22*, 1894–1903.

Martín-Arévalo, E., Chica, A.B., and Lupiáñez, J. (2016). No single electrophysiological marker for facilitation and inhibition of return: A review. Behav. Brain Res. *300*, 1–10.

Mesulam, M.M. (2000). Principles of behavioral and cognitive neurology (New York, NY: Oxford University Press).

Mirpour, K., Arcizet, F., Ong, W.S., and Bisley, J.W. (2009). Been there, seen that: a neural mechanism for performing efficient visual search. J. Neurophysiol. *102*, 3481–3491.

Mirpour, K., Bolandnazar, Z., and Bisley, J.W. (2019). Neurons in FEF Keep Track of Items That Have Been Previously Fixated in Free Viewing Visual Search. J. Neurosci. *39*, 2114–2124.

Moore, T., and Armstrong, K.M. (2003). Selective gating of visual signals by microstimulation of frontal cortex. Nature *421*, 370–373.

Moore, T., and Zirnsak, M. (2017). Neural Mechanisms of Selective Visual Attention. Annu. Rev. Psychol. *68*, 47–72.

Mukamel, R., and Fried, I. (2012). Human intracranial recordings and cognitive neuroscience. Annu. Rev. Psychol. *63*, 511–537.

Murray, J.D., Bernacchia, A., Freedman, D.J., Romo, R., Wallis, J.D., Cai, X., Padoa-Schioppa, C., Pasternak, T., Seo, H., Lee, D., et al. (2014). A hierarchy of intrinsic timescales across primate cortex. Nat. Neurosci. *17*, 1661–1663.

Oostenveld, R., Fries, P., Maris, E., and Schoffelen, J.-M. (2011). FieldTrip: Open source software for advanced analysis of MEG, EEG, and invasive electrophysiological data. Comput. Intell. Neurosci. *2011*, 156869.

Parvizi, J., and Kastner, S. (2018). Promises and limitations of human intracranial electroencephalography. Nat. Neurosci. *21*, 474–483.

Patel, G.H., Yang, D., Jamerson, E.C., Snyder, L.H., Corbetta, M., and Ferrera, V.P. (2015). Functional evolution of new and expanded attention networks in humans. Proc. Natl. Acad. Sci. U. S. A. *112*, 9454–9459.

Pérez-García, F., Lehongre, K., Bardinet, E., Jannin, P., and Fernandez-Vidal, S. (2015). Automatic Segmentation Of Depth Electrodes Implanted In Epileptic Patients: A Modular Tool Adaptable To Multicentric Protocols. *56*.

Poffenberger, A.T. (1912). Reaction time to retinal stimulation: with special reference to the time lost in conduction through nerve centers.

Posner, M.I., and Cohen, Y. (1984). Components of visual orienting. In Attention and Performance X: Control of Language Processes, H. Bouma, and D. Bouwhuis, eds. (Hillsdale, NJ: Erlbaum), pp. 531–56.

Ray, S., and Maunsell, J.H.R. (2011). Different origins of gamma rhythm and high-gamma activity in macaque visual cortex. PLoS Biol. *9*, e1000610.

Ro, T., Farnè, A., and Chang, E. (2003). Inhibition of return and the human frontal eye fields. Exp. Brain Res. *150*, 290–296.

Rosenke, M., van Hoof, R., van den Hurk, J., Grill-Spector, K., and Goebel, R. (2021). A Probabilistic Functional Atlas of Human Occipito-Temporal Visual Cortex. Cereb. Cortex *31*, 603–619.

Sani, I., Stemmann, H., Caron, B., Bullock, D., Stemmler, T., Fahle, M., Pestilli, F., and Freiwald, W.A. (2021). The human endogenous attentional control network includes a ventro-temporal cortical node. Nat. Commun. *12*, 360.

Sapir, A., Soroker, N., Berger, A., and Henik, A. (1999). Inhibition of return in spatial attention: direct evidence for collicular generation. Nat. Neurosci. *2*, 1053–1054.

Seidel Malkinson, T., and Bartolomeo, P. (2018). Fronto-parietal organization for response times in inhibition of return: The FORTIOR model. Cortex *102*, 176–192.

Shallice, T. (1979). A Theory of Consciousness: Chronometric Explorations of Mind . Michael I. Posner. Erlbaum, Hillsdale, N.J., 1978 (distributor, Halsted [Wiley], New York). xvi, 272 pp., illus. $14.95. The Experimental Psychology Series. Science *204*, 827–827.

Siéroff, E., Decaix, C., Chokron, S., and Bartolomeo, P. (2007). Impaired orienting of attention in left unilateral neglect: A componential analysis. Neuropsychology *21*, 94–113.

Soltani, A., and Koch, C. (2010). Visual saliency computations: mechanisms, constraints, and the effect of feedback. J. Neurosci. *30*, 12831–12843.

Stemmann, H., and Freiwald, W.A. (2019). Evidence for an attentional priority map in inferotemporal cortex. Proc. Natl. Acad. Sci. U. S. A. *116*, 23797–23805.

Stigliani, A., Jeska, B., and Grill-Spector, K. (2017). Encoding model of temporal processing in human visual cortex. Proc. Natl. Acad. Sci. U. S. A. *114*, E11047–E11056.

Sydnor, V.J., Larsen, B., Bassett, D.S., Alexander-Bloch, A., Fair, D.A., Liston, C., Mackey, A.P., Milham, M.P., Pines, A., Roalf, D.R., et al. (2021). Neurodevelopment of the association cortices: Patterns, mechanisms, and implications for psychopathology. Neuron *109*, 2820–2846.

Szczepanski, S.M., and Kastner, S. (2013). Shifting attentional priorities: control of spatial attention through hemispheric competition. Journal of Neuroscience *33*, 5411–5421.

Taylor, T.L., and Klein, R.M. (2000). Visual and motor effects in inhibition of return. J. Exp. Psychol. Hum. Percept. Perform. *26*, 1639–1656.

Team, Jasp (2020). JASP (Version 0.14.1)[Computer software].

Thiebaut de Schotten, M., Urbanski, M., Duffau, H., Volle, E., Levy, R., Dubois, B., and Bartolomeo, P. (2005). Direct evidence for a parietal-frontal pathway subserving spatial awareness in humans. Science *309*, 2226–2228.

Thiebaut de Schotten, M., Dell'Acqua, F., Forkel, S.J., Simmons, A., Vergani, F., Murphy, D.G.M., and Catani, M. (2011). A lateralized brain network for visuospatial attention. Nat. Neurosci. *14*, 1245–1246.

Thompson, K.G., and Bichot, N.P. (2005). A visual salience map in the primate frontal eye field. Prog. Brain Res. *147*, 251–262.

VanRullen, R. (2005). Visual Saliency and Spike Timing in the Ventral Visual Pathway. Neurobiology of Attention 272–278.

Veale, R., Hafed, Z.M., and Yoshida, M. (2017). How is visual salience computed in the brain? Insights from behaviour, neurobiology and modelling. Philos. Trans. R. Soc. Lond. B Biol. Sci. *372*.

Vernet, M., Quentin, R., Chanes, L., Mitsumasu, A., and Valero-Cabré, A. (2014). Frontal eye field, where art thou? Anatomy, function, and non-invasive manipulation of frontal regions involved in eye movements and associated cognitive operations. Front. Integr. Neurosci. *8*, 66.

Vu, A.T., Auerbach, E., Lenglet, C., Moeller, S., Sotiropoulos, S.N., Jbabdi, S., Andersson, J., Yacoub, E., and Ugurbil, K. (2015). High resolution whole brain diffusion imaging at 7T for the Human Connectome Project. Neuroimage *122*, 318–331.

Wang, F., Chen, M., Yan, Y., Zhaoping, L., and Li, W. (2015). Modulation of Neuronal Responses by Exogenous Attention in Macaque Primary Visual Cortex. J. Neurosci. *35*, 13419–13429.

Wasmuht, D.F., Spaak, E., Buschman, T.J., Miller, E.K., and Stokes, M.G. (2018). Intrinsic neuronal dynamics predict distinct functional roles during working memory. Nat. Commun. *9*, 3499.

Zhaoping, L. (2016). From the optic tectum to the primary visual cortex: migration through evolution of the saliency map for exogenous attentional guidance. Curr. Opin. Neurobiol. *40*, 94–102.

Zhou, J., Benson, N.C., Kay, K.N., and Winawer, J. (2018). Compressive Temporal Summation in Human Visual Cortex. J. Neurosci. *38*, 691–709.

Acknowledgments: We would like to thank Pietro Avanzini, Danilo Bzdok, Florence Bouhali, and the PICNIC lab at the ICM for invaluable discussions and assistance.

Funding:

Israel Science Foundation postdoctoral fellowship number 57/15 (TSM)

Marie Sklodowska Curie fellowship 702577-DynamAtt (TSM)

Agence Nationale de la Recherche BRANDY grant ANR-16-CE37-0005 (TSM, DJB, VN, SFV, PB)

Author contributions:

Conceptualization: TSM, DJB, PB

Data curation: KL

Formal analysis: TSM

Methodology: TSM, JDS, BCK, JL

Investigation: TSM, DJB

Visualization: TSM, BCK

Funding acquisition: TSM, PB

Project administration: TSM

Resources: KL, SFV, VN, CA, VL, DSM

Software: TSM, DJB, AB, JDS, SFV, DSM

Supervision: PB

Writing – original draft: TSM

Writing – review & editing: TSM, DJB, BCK, AB, KL, SFV, VN, CA, VL, DSM, JDS, PB

Competing interests: Authors declare that they have no competing interests.

Supplementary Materials

Supplementary results

Figs. S1 to S10

Table S1 S2

Movies S1 to S2

Patient #	Age	Gender	Handedness	Number of electrodes (total 243)	Total number of contacts (total 1,884)	Implanted hemisphere
1	49	M	R	10	104	RH
2	44	F	R	12	96	LH+RH
3	31	M	R	12	82	RH
4	31	F	R	10	82	LH
5	26	M	R	9	58	RH
6	47	M	R	11	90	LH
7	31	F	R	9	54	LH
8	30	M	R	9	63	LH
9	26	M	L+R	10	44	LH+RH
10	24	M	R	9	48	LH
11	26	F	R	10	88	LH
12	22	F	R	10	58	RH
13	34	F	R	8	76	LH
14	40	F	R	7	62	LH
15	34	M	R	10	70	LH+RH
16	45	F	R	9	78	LH+RH
17	24	F	R	8	61	RH
18	19	M	R	7	65	RH
19	34	M	R	7	31	RH
20	47	M	R	8	53	LH
21	31	F	L	8	56	LH
22	31	M	L	5	48	LH
23	26	F	R	8	63	RH
24	26	F	R	9	77	RH
25	31	F	R	9	67	LH+RH
26	21	F	R	9	54	LH+RH
27	30	F	R	12	93	RH
28	28	M	R	11	62	LH
Mean	**31.7±8.1**	**54% F**	**89% R**	**9.1**	**67.3**	**57% RH**

Table 1 *– Implanted patients demographic details*

Region name	Responsive Electrodes N	Cluster 1 N	Cluster 2 N	Cluster 3 N
Banks superior temporal sulcus	9	1	4	1
Caudal anterior-cingulate cortex	3	0	0	0
Caudal middle frontal gyrus	12	2	2	1
Entorhinal cortex	6	0	0	0
Fusiform gyrus Posterior	33	7	8	3
Fusiform gyrus Med	14	2	2	0
Fusiform gyrus Anterior	10	0	0	0
Inferior parietal cortex	51	19	14	5
Inferior temporal gyrus Posterior	28	1	8	1
Inferior temporal gyrus Middle	14	0	3	0
Inferior temporal gyrus Antrior	13	0	0	0
Lateral occipital cortex	20	6	5	2
Lingual gyrus	17	1	0	3
Medial orbital frontal cortex	4	0	0	0
Middle temporal gyrus Posterior	37	10	12	1
Middle temporal gyrus Middle	19	0	2	0
Middle temporal gyrus Anterior	35	0	0	0
Parahippocampal gyrus	8	0	0	0
Paracentral lobule	1	0	0	0
Pars opercularis	8	0	0	1
Pars orbitalis	36	0	0	0
Pars triangularis	9	0	0	4
Pericalcarine cortex	1	0	0	0
Postcentral gyrus dorsal	1	0	0	0
Postcentral gyrus ventral	1	0	0	0
Posterior-cingulate cortex	3	0	1	1
Precentral gyrus dorsal	16	6	3	4
Precentral gyrus ventral	5	0	3	1
Precuneus cortex	1	0	0	0
Rostral middle frontal gyrus	16	0	4	2
Superior frontal gyrus	46	0	8	16
Superior parietal cortex	10	1	3	1
Superior temporal gyrus Posterior	19	2	1	3
Superior temporal gyrus Middle	17	0	0	0
Superior temporal gyrus Anterior	13	0	0	3
Supramarginal gyrus	22	0	3	9
Temporal pole	14	0	0	0
White matter	49	10	10	5
hippocampus	18	0	1	0
amygdala	5	0	0	0

Table 2 *– Responsive electrodes localization according to the Desikan-Killiany-Tourville atlas* (Desikan et al., 2006)

Cluster	Effect	Cue Time-Window - Time from target onset [s]																													
		0.6	0.58	0.56	0.54	0.52	0.5	0.48	0.46	0.44	0.42	0.4	0.38	0.36	0.34	0.32	0.3	0.28	0.26	0.24	0.22	0.2	0.18	0.16	0.14	0.12	0.1	0.08	0.06	0.04	0.02	0
1	Hemisphere	0.000	1.000	0.003	0.003	0.025	0.044	1.000	0.141	1.000	1.000	0.009	0.007	1.000	0.309	0.121	1.000	0.004	0.010	0.062	0.008	0.038	0.174	0.074	0.208	1.000	1.000	0.061	0.003	0.908	1.000	1.000
	Congruence	1.000	1.000	1.000	1.000	1.000	1.000	0.055	1.000	1.000	1.000	1.000	1.000	1.000	1.000	1.000	1.000	1.000	1.000	1.000	1.000	1.000	1.000	1.000	1.000	0.013	1.000	1.000	1.000	1.000	1.000	1.000
	Laterality	0.002	0.459	1.000	1.000	0.234	1.000	0.965	0.013	0.511	1.000	1.000	0.000	0.004	0.232	0.003	0.000	0.000	0.000	0.002	0.344	0.134	1.000	1.000	0.592	0.010	0.000	1.000	1.000	0.592	0.004	1.000
	Hem * Cong	1.000	1.000	1.000	1.000	1.000	1.000	1.000	1.000	1.000	1.000	1.000	1.000	1.000	1.000	0.707	1.000	0.387	1.000	1.000	1.000	1.000	0.662	1.000	0.913	1.000	1.000	1.000	0.708	1.000	1.000	1.000
	Hem * Laterality	1.000	0.187	0.273	1.000	1.000	1.000	1.000	1.000	1.000	1.000	1.000	0.009	1.000	1.000	1.000	1.000	1.000	1.000	1.000	1.000	1.000	1.000	1.000	1.000	1.000	0.174	0.092	1.000	1.000	1.000	0.445
	Cong * Laterality	1.000	0.018	0.000	0.000	0.000	0.000	0.000	0.000	0.000	0.000	0.000	0.000	0.003	0.847	1.000	1.000	0.437	1.000	1.000	1.000	0.847	1.000	0.002	0.001	0.000	0.000	0.018	0.010	0.143	0.000	0.000
	Hem * Cong * Laterality	1.000	1.000	1.000	1.000	1.000	1.000	1.000	1.000	1.000	0.541	0.044	0.503	1.000	1.000	1.000	0.769	1.000	1.000	0.719	1.000	1.000	0.136	1.000	1.000	1.000	1.000	1.000	1.000	1.000	1.000	1.000
2	Hemisphere	1.000	1.000	0.643	0.182	1.000	1.000	1.000	1.000	1.000	1.000	1.000	1.000	1.000	0.697	0.355	0.152	1.000	1.000	1.000	1.000	0.666	1.000	1.000	1.000	1.000	0.153	1.000	1.000	1.000	0.805	1.000
	Congruence	1.000	1.000	1.000	1.000	1.000	1.000	1.000	1.000	1.000	1.000	1.000	1.000	1.000	1.000	1.000	1.000	1.000	1.000	1.000	1.000	1.000	1.000	1.000	1.000	1.000	1.000	1.000	1.000	1.000	1.000	1.000
	Laterality	0.036	0.000	0.010	1.000	1.000	1.000	1.000	1.000	1.000	1.000	0.643	0.814	1.000	1.000	0.113	1.000	1.000	0.582	1.000	1.000	0.076	1.000	1.000	0.498	1.000	0.128	1.000	1.000	1.000	1.000	1.000
	Hem * Cong	1.000	1.000	1.000	1.000	1.000	1.000	1.000	1.000	1.000	1.000	1.000	1.000	1.000	1.000	1.000	1.000	1.000	1.000	1.000	1.000	0.227	1.000	1.000	1.000	1.000	1.000	1.000	1.000	1.000	1.000	1.000
	Hem * Laterality	1.000	0.746	1.000	1.000	1.000	1.000	1.000	1.000	1.000	1.000	1.000	1.000	1.000	1.000	1.000	1.000	1.000	1.000	1.000	1.000	1.000	1.000	1.000	1.000	1.000	1.000	1.000	1.000	1.000	1.000	1.000
	Cong * Laterality	0.065	0.096	1.000	1.000	1.000	0.009	0.000	0.000	0.000	0.000	0.000	0.000	0.000	0.000	0.000	0.000	0.165	0.096	1.000	0.368	0.005	0.199	1.000	0.365	0.118	0.089	0.418	0.038	0.299	0.534	0.119
	Hem * Cong * Laterality	1.000	1.000	1.000	1.000	1.000	1.000	1.000	1.000	1.000	1.000	1.000	1.000	0.026	0.527	1.000	1.000	1.000	1.000	1.000	1.000	1.000	1.000	1.000	1.000	1.000	1.000	1.000	1.000	1.000	1.000	1.000
3	Hemisphere	0.366	1.000	1.000	1.000	1.000	1.000	1.000	0.011	0.025	0.619	0.460	1.000	1.000	1.000	0.001	1.000	0.427	0.013	0.001	0.001	0.190	0.022	0.056	1.000	0.002	0.050	1.000	1.000	1.000	1.000	1.000
	Congruence	1.000	1.000	1.000	1.000	1.000	1.000	1.000	1.000	1.000	1.000	1.000	1.000	1.000	1.000	1.000	1.000	1.000	1.000	1.000	1.000	1.000	1.000	1.000	1.000	1.000	1.000	0.763	1.000	1.000	0.228	1.000
	Laterality	1.000	0.577	1.000	1.000	1.000	1.000	1.000	1.000	1.000	1.000	0.089	0.252	1.000	1.000	1.000	1.000	1.000	1.000	0.980	1.000	1.000	1.000	1.000	1.000	1.000	1.000	1.000	1.000	0.759	0.318	1.000
	Hem * Cong	1.000	0.178	0.369	1.000	1.000	1.000	1.000	1.000	1.000	1.000	1.000	1.000	1.000	1.000	1.000	1.000	0.648	0.782	1.000	1.000	1.000	1.000	1.000	1.000	1.000	1.000	0.710	0.045	0.000	0.782	1.000
	Hem * Laterality	1.000	1.000	1.000	1.000	1.000	1.000	0.278	1.000	1.000	1.000	1.000	1.000	1.000	1.000	1.000	1.000	1.000	0.621	1.000	0.404	1.000	1.000	1.000	1.000	1.000	1.000	1.000	1.000	1.000	1.000	1.000
	Cong * Laterality	1.000	1.000	1.000	1.000	1.000	1.000	0.219	1.000	0.243	0.076	1.000	1.000	1.000	0.198	1.000	1.000	1.000	1.000	1.000	1.000	1.000	1.000	1.000	1.000	1.000	1.000	1.000	1.000	1.000	1.000	1.000
	Hem * Cong * Laterality	1.000	1.000	1.000	1.000	1.000	1.000	1.000	1.000	1.000	0.641	1.000	1.000	1.000	1.000	1.000	1.000	1.000	1.000	1.000	1.000	1.000	1.000	1.000	1.000	1.000	1.000	1.000	1.000	1.000	1.000	1.000

Table S1 *– IOR-related neural activity in the cue time-window. Holm corrected p-values for the 3-way ANOVA testing the effects of Congruence, Hemisphere and Target laterality on the HFBB signal in the long SOA condition in the Early (yellow), Middle (red) and Late (green) clusters. Significant effects in shaded yellow.*

Cluster	Effect	Target Time-Window - Time from target onset [s]																																											
		0.00	0.02	0.04	0.06	0.08	0.10	0.12	0.14	0.16	0.18	0.20	0.22	0.24	0.26	0.28	0.30	0.32	0.34	0.36	0.38	0.40	0.42	0.44	0.46	0.48	0.50	0.52	0.54	0.56	0.58	0.60	0.62	0.64	0.66	0.68	0.70	0.72	0.74	0.76	0.78	0.80
1	Hemisphere	1.00	1.00	1.00	1.00	0.00	0.00	0.02	0.14	0.00	1.00	1.00	1.00	1.00	1.00	1.00	1.00	1.00	1.00	0.37	1.00	1.00	0.53	0.10	0.09	0.00	0.03	1.00	1.00	1.00	1.00	1.00	1.00	1.00	0.05	0.05	1.00	1.00	1.00	1.00	1.00	1.00
	Congruence	1.00	1.00	1.00	1.00	0.36	0.33	1.00	1.00	1.00	1.00	1.00	1.00	1.00	1.00	1.00	1.00	1.00	1.00	1.00	1.00	0.26	1.00	1.00	0.42	1.00	1.00	1.00	1.00	1.00	1.00	1.00	1.00	1.00	1.00	1.00	1.00	1.00	1.00	1.00	1.00	1.00
	Laterality	1.00	1.00	1.00	0.00	0.00	0.00	0.00	0.00	0.00	0.00	0.00	0.00	0.00	0.00	0.08	0.02	1.00	1.00	1.00	1.00	1.00	1.00	1.00	1.00	0.03	0.01	1.00	1.00	1.00	1.00	1.00	0.02	0.19	1.00	1.00	1.00	0.94	1.00	0.35	0.00	1.00
	Hem * Cong	1.00	1.00	1.00	1.00	1.00	1.00	1.00	1.00	1.00	1.00	1.00	1.00	1.00	1.00	0.51	1.00	1.00	1.00	1.00	1.00	1.00	1.00	1.00	0.46	1.00	1.00	1.00	1.00	1.00	0.41	1.00	1.00	1.00	1.00	1.00	1.00	1.00	1.00	1.00	1.00	1.00
	Hem * Laterality	0.74	1.00	1.00	1.00	1.00	1.00	1.00	1.00	1.00	1.00	1.00	1.00	0.02	0.00	0.59	0.00	0.47	1.00	1.00	1.00	1.00	1.00	1.00	1.00	1.00	1.00	1.00	1.00	1.00	1.00	1.00	1.00	1.00	1.00	0.72	1.00	1.00	1.00	1.00	1.00	1.00
	Cong * Laterality	0.00	0.00	0.01	0.04	0.11	0.00	0.01	1.00	0.72	0.07	1.00	1.00	1.00	1.00	1.00	1.00	1.00	0.02	0.00	0.42	0.03	1.00	1.00	1.00	1.00	1.00	1.00	1.00	1.00	1.00	1.00	1.00	1.00	1.00	1.00	1.00	1.00	1.00	1.00	1.00	1.00
	Hem * Cong * Laterality	1.00	1.00	1.00	1.00	1.00	1.00	1.00	1.00	1.00	1.00	1.00	1.00	1.00	0.05	1.00	1.00	1.00	1.00	1.00	1.00	0.95	1.00	1.00	1.00	1.00	1.00	1.00	1.00	1.00	1.00	1.00	1.00	1.00	1.00	1.00	1.00	1.00	1.00	1.00	1.00	1.00
2	Hemisphere	1.00	1.00	1.00	1.00	0.77	1.00	1.00	1.00	1.00	1.00	0.77	0.28	1.00	1.00	1.00	0.27	1.00	0.56	0.08	0.22	1.00	0.99	0.56	0.70	0.02	0.00	0.32	1.00	1.00	1.00	1.00	0.95	0.32	0.99	1.00	1.00	1.00	1.00	1.00	1.00	1.00
	Congruence	1.00	1.00	1.00	1.00	1.00	1.00	1.00	1.00	1.00	1.00	1.00	1.00	0.00	0.00	0.00	0.10	1.00	1.00	1.00	1.00	1.00	1.00	1.00	1.00	1.00	1.00	1.00	1.00	1.00	1.00	1.00	1.00	1.00	1.00	1.00	1.00	0.09	1.00	1.00	1.00	1.00
	Laterality	1.00	1.00	1.00	1.00	1.00	0.16	0.02	0.00	0.00	0.00	0.00	0.00	0.00	0.00	0.01	0.00	0.25	0.48	1.00	1.00	0.01	0.71	1.00	1.00	1.00	1.00	1.00	1.00	1.00	1.00	1.00	1.00	1.00	0.01	1.00	0.41	1.00	1.00	1.00	1.00	1.00
	Hem * Cong	1.00	1.00	1.00	1.00	1.00	1.00	1.00	0.04	0.00	0.01	1.00	0.83	1.00	1.00	1.00	1.00	1.00	1.00	1.00	1.00	1.00	1.00	1.00	1.00	1.00	1.00	1.00	1.00	1.00	1.00	1.00	1.00	1.00	1.00	1.00	1.00	1.00	1.00	1.00	1.00	1.00
	Hem * Laterality	1.00	1.00	1.00	1.00	1.00	1.00	1.00	1.00	1.00	1.00	0.01	0.14	0.27	1.00	1.00	1.00	0.90	1.00	1.00	1.00	1.00	1.00	1.00	1.00	1.00	1.00	1.00	1.00	1.00	1.00	1.00	1.00	1.00	1.00	1.00	1.00	1.00	1.00	1.00	1.00	1.00
	Cong * Laterality	0.40	0.95	0.27	0.61	1.00	0.03	1.00	1.00	1.00	1.00	0.07	1.00	1.00	1.00	1.00	1.00	1.00	1.00	1.00	1.00	1.00	1.00	0.07	1.00	1.00	1.00	1.00	1.00	1.00	1.00	1.00	1.00	1.00	1.00	1.00	1.00	1.00	1.00	1.00	1.00	1.00
	Hem * Cong * Laterality	1.00	1.00	1.00	1.00	1.00	1.00	1.00	1.00	1.00	1.00	1.00	1.00	1.00	1.00	1.00	1.00	0.88	1.00	1.00	1.00	1.00	1.00	1.00	1.00	1.00	1.00	1.00	1.00	1.00	1.00	1.00	1.00	1.00	1.00	1.00	1.00	1.00	1.00	1.00	1.00	1.00
3	Hemisphere	1.00	1.00	1.00	1.00	1.00	1.00	0.34	0.00	0.00	0.00	0.00	0.00	0.00	0.00	1.00	1.00	1.00	1.00	0.18	1.00	0.04	0.20	0.14	0.22	0.25	0.00	1.00	1.00	1.00	0.03	0.91	1.00	0.01	0.00	0.62	1.00	1.00	1.00	1.00	1.00	0.87
	Congruence	1.00	1.00	1.00	1.00	1.00	1.00	1.00	1.00	1.00	1.00	1.00	1.00	1.00	0.98	1.00	1.00	1.00	1.00	1.00	1.00	1.00	0.98	0.07	1.00	1.00	1.00	0.79	1.00	0.20	1.00	1.00	1.00	1.00	0.00	1.00	1.00	1.00	0.22	1.00	1.00	1.00
	Laterality	1.00	1.00	1.00	1.00	1.00	1.00	1.00	1.00	1.00	1.00	1.00	0.02	0.03	0.01	0.00	0.01	0.06	1.00	1.00	1.00	0.82	1.00	1.00	1.00	1.00	1.00	1.00	1.00	1.00	1.00	1.00	1.00	1.00	1.00	1.00	1.00	1.00	1.00	1.00	1.00	1.00
	Hem * Cong	1.00	1.00	1.00	1.00	1.00	1.00	1.00	1.00	1.00	1.00	1.00	1.00	1.00	0.47	1.00	0.76	1.00	1.00	1.00	1.00	1.00	1.00	1.00	1.00	0.88	1.00	1.00	1.00	1.00	1.00	1.00	1.00	1.00	1.00	1.00	1.00	1.00	1.00	1.00	1.00	1.00
	Hem * Laterality	1.00	1.00	0.01	0.02	1.00	1.00	1.00	1.00	1.00	1.00	1.00	0.09	1.00	1.00	1.00	1.00	1.00	1.00	1.00	1.00	1.00	1.00	1.00	1.00	1.00	1.00	1.00	1.00	1.00	1.00	1.00	1.00	1.00	1.00	1.00	1.00	1.00	1.00	1.00	1.00	1.00
	Cong * Laterality	1.00	1.00	1.00	1.00	0.18	1.00	1.00	1.00	1.00	1.00	1.00	1.00	1.00	1.00	1.00	1.00	1.00	1.00	1.00	1.00	1.00	1.00	1.00	1.00	1.00	1.00	1.00	1.00	1.00	1.00	1.00	1.00	1.00	1.00	1.00	1.00	1.00	1.00	1.00	1.00	1.00
	Hem * Cong * Laterality	1.00	1.00	1.00	1.00	1.00	1.00	1.00	1.00	1.00	1.00	1.00	1.00	1.00	0.24	1.00	1.00	1.00	1.00	1.00	1.00	1.00	1.00	1.00	1.00	1.00	1.00	1.00	1.00	1.00	1.00	1.00	1.00	1.00	1.00	1.00	1.00	1.00	1.00	1.00	1.00	1.00

Table S2 *– IOR-related neural activity in the Target time-window. Holm corrected p-values for the 3-way ANOVA testing the effects of Congruence, Hemisphere and Target laterality on the HFBB signal in the long SOA condition in the Early (yellow), Middle (red) and Late (green) clusters. Significant effects in shaded yellow.*

Supplementary Results

Clusters' hemispheric lateralization

To test if the clusters' spatial distribution differs between right and left hemispheres, we performed a χ^2 analysis only in symmetrically covered regions (see methods), that revealed a significant lateralization ($X^2(5)=29.09$, $p<0.001$). Post hoc comparisons showed that this effect resulted from a significant right lateralization of Cluster 2 and a significant left lateralization of Cluster 3 (post hoc binomial tests, p=0.01 and p=0.003).

Cue time-window long-SOA effects

Cluster 1 responded only for contralateral cues (Congruence x Laterality interaction: -580 to -360ms, -180 to -60ms, -40 – 0ms pre target; largest *p*=0.038; see Fig. S6), reflecting the presence of a cue contralateral to the recording contact only in Incongruent contralateral and Congruent ipsilateral target trials, and demonstrating the visual processing properties of this cluster. Cluster 2 responded to both contralateral and ipsilateral cues but with stronger responses for cues presented contralaterally to the recording contact and with a later latency than in Cluster 1, demonstrating this cluster's spatial sensitivty (Congruence x Laterality interaction: -520 to -300ms, -220 to -200ms, -80 to -60ms pre target onset; largest *p*=0.03). Clusters 1 and 2 also showed a short triple interaction effect, (Congruence x Laterality x Hemisphere interaction; Cluster 1: -420 to -400ms; largest *p*=0.044; Cluster 2: -380 to -360ms; largest *p*=0.026). Congruence x Laterality interaction effect did not reach significance in Cluster 3, yet this cluster showed slightly stronger response for Incongruent trials compared to Congruent trials in the left hemisphere more than in the right hemisphere (Congruence x Hemisphere interaction: -80 to -40ms pre target onset; largest *p*=0.046).

Cross correlation of target-locked activity

To validate the association between cluster neural activity timing and RT we calculated the cross-correlation of target-locked neural activity across RT-bins. We computed the cross-correlation between activity at the fastest RT-bin and all subsequent bins in each condition for each cluster. If cluster activity is target-associated, maximal cross-correlation will be centered on target onset, resulting in a zero shift across all RT bins (Fig. S7). If cluster activity is response-associated, maximal cross-correlation will follow the RT, resulting in a negative shift of cross-correlation lag. To test if the lag in which the cross correlation was maximal corresponded to the RT we calculated the Pearson correlation between them. In Cluster 1, cross-correlation coefficients were centered on zero, and there was no correlation between the maximal lag and RT, suggesting that Cluster 1 activity is target-associated. In Cluster 2 and 3, cross-correlation coefficients showed a negative shifted lag that was generally correlated with RT, indicating that these clusters are response-associated.

Cross correlation of response-locked activity

To validate the association between cluster neural activity timing and target onset time we calculated the cross-correlation of response-locked neural activity across RT-bins. We computed the cross-correlation between activity at the fastest RT-bin and all subsequent bins in each condition for each cluster. If cluster activity is target-associated, maximal cross-correlation will follow the RT (here indicative of quantile's mean target-onset time), resulting in a positive shift of cross-correlation lag (Fig. S9). If cluster activity is response-associated, maximal cross-correlation will be centered on target onset, resulting in a zero shift across all RT

bins. To test if the lag in which the cross correlation was maximal corresponded to target onset we calculated the Pearson correlation between the lag and RT. In RT-Cluster 1 and RT-Cluster 2a, cross-correlation coefficients were positively shifted in a spatially sensitive manner, i.e. only for contralateral targets and there were significant ($p<0.05$) positive correlations, only for contralateral targets, indicating that their activity showed visual modulation. In RT-Cluster 2b and RT-Cluster 3, cross-correlation coefficients showed no shift and were not correlated with the RT, thus their activity is response-associated.